

Copper–Cystine Biohybrid-Embedded Nanofiber Aerogels Show Antibacterial and Angiogenic Properties

Anik Karan,[○] Navatha Shree Sharma,[○] Margarita Darder, Yajuan Su, Syed Muntazir Andrabi, S M Shatil Shahriar, Johnson V. John, Zeyu Luo, Mark A. DeCoster, Yu Shrike Zhang, and Jingwei Xie*



Cite This: *ACS Omega* 2024, 9, 9765–9781



Read Online

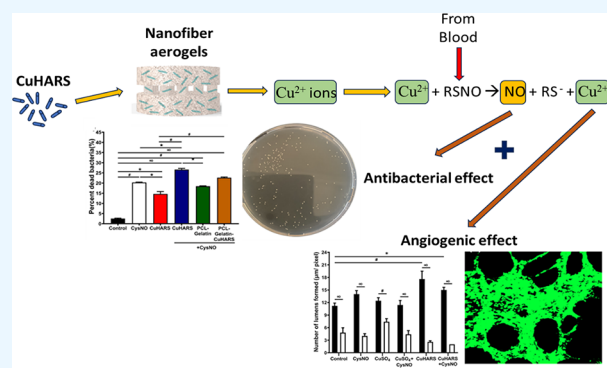
ACCESS |

Metrics & More

Article Recommendations

Supporting Information

ABSTRACT: Copper–cystine-based high aspect ratio structures (CuHARS) possess exceptional physical and chemical properties and exhibit remarkable biodegradability in human physiological conditions. Extensive testing has confirmed the biocompatibility and biodegradability of CuHARS under diverse biological conditions, making them a viable source of essential Cu^{2+} . These ions are vital for catalyzing the production of nitric oxide (NO) from the decomposition of S-nitrosothiols (RSNOs) found in human blood. The ability of CuHARS to act as a Cu^{2+} donor under specific concentrations has been demonstrated in this study, resulting in the generation of elevated levels of NO. Consequently, this dual function makes CuHARS effective as both a bactericidal agent and a promoter of angiogenesis. *In vitro* experiments have shown that CuHARS actively promotes the migration and formation of complete lumens by redirecting microvascular endothelial cells. To maximize the benefits of CuHARS, they have been incorporated into biomimetic electrospun poly(ϵ -caprolactone)/gelatin nanofiber aerogels. Through the regulated release of Cu^{2+} and NO production, these channeled aerogels not only provide antibacterial support but also promote angiogenesis. Taken together, the inclusion of CuHARS in biomimetic scaffolds could hold great promise in revolutionizing tissue regeneration and wound healing.



1. INTRODUCTION

Copper is an essential trace element required in living organisms and a cofactor in several enzymes like tyrosinase, cytochrome c oxidase, or superoxide dismutase, acting as an electron donor/acceptor by alternating between Cu(I) and Cu(II) redox states.^{1–3} The interaction of copper with biologically relevant compounds such as amino acids and other ligands is a topic of interest due to the role of copper ions in some biochemical processes, as well as for possible application as anticancer agents, contrast agents in nuclear magnetic resonance (NMR) imaging, and its antifungal activity.^{4–6} Several studies focused on the interaction of copper ions with the biologically occurring disulfide L-cystine, which results from the oxidation of the amino acid cystine with the formation of a disulfide bridge. Among them, Kahler et al. reported the formation of copper–cystine complexes with fiber morphology and showed a 1:1 stoichiometry on Formvar-coated copper screens at neutral pH values.⁷ They suggested that the formation of these fibers could give rise to artifacts when using copper screens in electron microscopy. Although this preliminary study stated that the fibers were not formed in an aqueous solution, this fact was later refuted by other reports.^{8–10} Hawkins and Perrin reported the formation of linear polynuclear complexes and studied their stability.⁸ Later,

Gale and Winkler prepared Cu–cystine complexes at temperatures below 40 °C and at boiling temperatures, obtaining a pale blue-violet precipitate at lower temperatures and a light green material at higher temperatures. They suggested that L-cystine may adopt different crystal structural conformations, but a possible structure was not proposed.⁹ More recently, DeCoster and co-workers reported the formation of Cu–L-cystine fibers in cell culture media while studying the toxicity of CuO nanoparticles, and later the synthesis was optimized from CuO nanoparticles or copper sulfate solutions.^{10–12} However, the exact structure of this fibrous material is still unknown.

Nowadays, the potential use of biological molecules as building units in metal–organic frameworks (MOFs) has created novel avenues for exploring fresh architectures and functionalities, particularly in catalysis, biosensing, and biomedical applications.¹³ Numerous studies have reported

Received: December 14, 2023

Revised: January 15, 2024

Accepted: February 1, 2024

Published: February 16, 2024



the creation of bioMOFs using amino acids or oligopeptides, resulting in flexible or robust frameworks depending on the bioligand.^{14–18} While the frameworks generally showcase microporosity, the selection of these bioligands stems from their hydrophilic or hydrophobic nature, the intrinsic chirality, the presence of additional metal-binding groups (carboxylate, amine, imidazole, thiol, or phenol groups), and the potential application of the resultant materials in areas like gas storage, separation of chiral molecules, heterogeneous catalysis, sensing or drug delivery.¹⁸ Most of the peptide-based bio-MOFs reported until now involve peptides consisting of two amino acids, like those based on glycylglutamic acid, glycylalanine, and the natural dipeptide carnosine (β -alanyl-L-histidine).^{19–21} Among them, some copper-containing bio-MOFs have been reported, like those based on the dimer glycylhistidine as a ligand or a derivative of the dipeptide L-phenylalanine–L-phenylalanine.^{22,23} In this context, the current work presents a new approach to synthesizing the Cu–L-cystine biohybrid, also known as copper high aspect ratio structures (CuHARS), aiming at unraveling its crystalline structure and how it can function as metal–organic biohybrids (MOBs), resembling existing MOFs in terms of their potential biomedical applications, by utilizing Cu²⁺ sourced from CuHARS.

Chronic wounds have been a major concern in clinics. The most common complications for chronic wounds are biofilm-associated infections, persistent inflammation due to immunomodulatory responses, and pain.^{24,25} Chronic wounds and associated complications account for 15% of the 8.2 million Medicare beneficiaries, resulting in costs ranging from \$28.1 to \$31.7 billion.^{26,27} The treatment of chronic wounds has been a subject of study for decades, with a crucial consideration being the insufficient formation of vascular tissues in the wound areas, resulting in notably slow wound healing.^{24,28,29} Rapid angiogenesis, which facilitates proper vascularization, along with controlled initial biofilm formation, are the two paramount factors considered in the study of tissue regeneration involved in wounds.^{30,31} Copper-based bioactive materials have been utilized for wound regeneration because of their antibacterial effect and promotion of angiogenesis. However, the critical factor is the targeted delivery of a nontoxic form of copper among many copper sources, including copper oxide nanoparticles and copper salts, which often exhibit substantial toxicity to structural cells even at extremely low concentrations.^{32–34} Another factor involves the development of a reliable delivery system capable of retaining bioactive materials for an extended duration. The system must also be biodegradable and emulate the extracellular matrix of wound tissue.^{35,36} Our study used a novel copper source known as CuHARS, demonstrating its potential as a catalyst for elevated angiogenesis and an antibacterial agent. Furthermore, CuHARS facilitated the generation of nitric oxide (NO) from S-nitrosothiols (RSNOs), which has also been shown as a crucial synergistic element for both angiogenesis and bactericidal effects.

The origin of NO is from RSNOs (hemoglobin and albumin-based) present in human blood. NO is enzymatically produced from L-arginine by specific NOS enzymes, particularly eNOS and NOS3, generated by endothelial cells.^{37–39} One of the primary concerns for NO is its stability.^{40,41} Due to its high reactivity, it has a very small half-life and once synthesized, it only persists for a few milliseconds. This brief duration is insufficient to support sustained angiogenesis. The role of NO in angiogenesis has

been a subject of study for decades. It modulates the behavior of endothelial cells by reducing apoptosis and enhancing proliferation. This effect is achieved by elevating the expression of vascular endothelial growth factor (VEGF) in areas of wounds or inflammation.^{39,42,43} NO mediates podokinesis by directing the vector of VEGF, resulting in the targeted migration of endothelial cells.⁴⁴ The most significant factor in promoting angiogenesis is the upregulation of eNOS in endothelial cells induced by the presence of NO. VEGF-mediated angiogenesis and vascular permeability function through eNOS. NO released by the enzymatic function of eNOS activates sGC-cGMP-PKG downstream signaling to promote angiogenesis. This research examined the impact of NO on human microvascular endothelial cells (HMEC1) and demonstrated its role in angiogenesis through *in vitro* studies. A simulated biological microenvironment akin to wound and inflammation was established by introducing S-nitrosothiol (CysNO) at concentrations comparable to those in the human blood into a culture of HMEC1 cells. The study illustrated the impact of catalyzing NO from RSNOs in the presence of the novel MOBs CuHARS. CuHARS have been a subject of research over the past few years, revealing their full biodegradability and minimal toxicity toward structural cells, such as rat brain microvascular endothelial cells, as evidenced by viability tests.^{45,46} CuHARS is regarded as a source of Cu²⁺ in the biological system. It has demonstrated a gradual degradation profile, releasing Cu²⁺ under passive biological conditions when examined in various brain cell culture media.^{12,45}

In this study, we investigated how the presence of Cu²⁺ catalyzes the breakdown of RSNOs into NO, promoting angiogenesis by extending the NO's presence in endothelial cells. This process facilitated the creation of complete lumens, making the initial stage in wound area blood vessel formation. Copper stimulation acts synergistically, aiding blood vessel development and maturation. Additionally, it triggers the activation of hypoxia-induced factor 1 (HIF-1), a crucial transcription factor regulating VEGF.^{32,47} The combined effect of copper and NO was also investigated to assess their collaborative impact on inhibiting initial bacterial growth as both copper and NO are recognized as antimicrobial agents. Copper is acknowledged for its antibacterial properties against both Gram-positive and Gram-negative bacteria, including *Escherichia coli* (*E. coli*) and *Staphylococcus aureus* (*S. aureus*).⁴⁸ Cu²⁺ tends to bind to bacterial membranes, inducing a bactericidal effect by upregulating reactive oxygen species (ROS). This process leads to lipid peroxidation of the membranes, protein oxidation, and DNA damage inside the bacterial cells.^{49–51} NO is also recognized for its potency, contributing to a broad-spectrum bactericidal effect. Moreover, NO has been reported to not induce bacterial resistance or be influenced by bacterial resistance over time.^{52,53} NO functions as a bactericidal reagent by upregulating oxidative and nitrosative stressors. This process leads to lipid peroxidation of bacterial membranes and nitrosation of membrane proteins. Ultimately, it induces DNA damage within bacteria through active nitrogen species like dinitrogen trioxide, peroxy nitrite, and many others.^{33,54,55}

2. MATERIALS AND METHODS

2.1. Materials. Poly(ϵ -caprolactone) (PCL) (80 kDa) and Type A gelatin from porcine skin, alginate lyase, anhydrous copper(II) sulfate, L-cysteine, L-cystine, and *tert*-butylnitrite

were purchased from Sigma-Aldrich (St. Louis, MO, USA). Glutaraldehyde (25% EtOH) solution was purchased from Thermo Fisher Scientific Inc., Waltham, MA, USA. Hexafluoroisopropanol (HFIP) was purchased from Oakwood Chemicals (Estill, SC, USA). Gibco (Thermo Fisher Scientific Inc., Waltham, MA, USA) supplied the fetal bovine serum (FBS), minimum necessary medium (MEM), and penicillin–streptomycin. The bacterial Live/Dead assay kit and Greiss assay kit were purchased from Thermo Fisher Scientific Inc., Waltham, MA, USA. Cell viability CCK-8 assay kit was obtained from Dojindo Laboratories, Rockville, MD, USA. Methicillin-resistant *S. aureus* (MRSA) USA300 LAC was obtained from the University of Nebraska Medical Center (UNMC). Luria–Bertani (LB) bacterial medium was purchased from Thermo Fisher Scientific Oxoid (Waltham, MA, USA).

2.2. Synthesis of CuHARS. The synthesis of CuHARS was carried out following the reported procedure.^{12,56} Briefly, L-cystine solution was prepared by dissolving 7.29 mg L-cystine in 100 μL of 0.1 M NaOH and then diluting 1 μL of L-cystine solution in 970 μL of sterile bidistilled water. The resultant solution was transferred to a closed container, preferably with a large surface area like a cell culture flask, and warmed for 30 min at 37 °C. Then, 32 μL of 2 mg/mL copper(II) sulfate solution was added to the flask, which was kept at 37 °C for 5 h. Subsequently, the flask was transferred to a refrigerator at 2–8 °C to form CuHARS. Finally, 3 μL of 0.1 M HCl was added per 1 mL of suspension, and the sample was recovered by centrifugation, rinsed twice with bidistilled water, and allowed to dry at 40 °C.

2.3. Characterization of CuHARS. Images of the CuHARS fibers were acquired using the optical microscope DMI6000B from Leica, FEI Quanta 200 scanning electron microscope (SEM) with attached EDS unit from Bruker and Hitachi H7500 transmission electron microscope (TEM). To determine the surface charge of the fibers, an aqueous 0.05% w/v CuHARS suspension (10 mL) was titrated to the point of zero charge with 0.001 N polydiallyldimethylammonium chloride (polyDADMAC), using the particle charge detector Mutek PCD-05 from BTG. The amount of organic components in the synthesized materials was determined by chemical analysis with a LECO CHNS 932 elemental analyzer. X-ray diffraction was carried out by a D8-ADVANCE diffractometer from Bruker, equipped with a LYNXEYE detector, and using the copper $K\alpha$ radiation. The voltage and current source were set at 40 kV and 30 mA, respectively. FTIR spectroscopy was carried out by a Bruker iFS 66VS spectrophotometer, and the samples were measured as KBr pellets between 4000 and 250 cm^{-1} with a resolution of 2 cm^{-1} . Raman spectroscopy was carried out using a green laser (514 nm) with a Renishaw inVia Raman microscope, which is coupled to a Leica DMLM microscope. UV–visible spectroscopy in the solid state was carried out using a UV-2401 PC spectrophotometer from Shimadzu equipped with an integrating sphere. The reflectance values were measured in the 800–200 nm wavelength range and then transformed to the corresponding absorbance data using the Kubelka–Munk function. The thermogravimetric analysis was carried out using a TGA Q50 instrument in the range from 25 to 600 °C with a heating rate of 10 °C/min under nitrogen flow. The water sorption properties were gravimetrically determined with an Aquadyne DVS dynamic water-vapor sorption analyzer from Quantachrome Instruments. The water sorption iso-

therms were obtained at 25 °C in the 0 to 95% relative humidity range, using an amount of sample around 10 mg. N_2 adsorption/desorption measurements were carried out at –196 °C on a Micromeritics ASAP 2010 analyzer, and the specific total surface area was determined using the Brunauer–Emmett–Teller (BET) method.

2.4. Fabrication of CuHARS-Embedded PCL/Gelatin Nanofiber Aerogels. The electrospinning was used to fabricate PCL/gelatin (1:1) mats. A spinning solution of 8% (w/v) PCL/gelatin was prepared by dissolving a predetermined mass of PCL and Gelatin in HFIP. A rotating mandrel was used to collect the aligned electrospun nanofibers used in this study. The following electrospinning parameters were used: DC voltage = 15 kV, flow rate = 0.4–0.6 mL/h, and distance between the collector and spinneret = 10–15 cm. The mats once produced were cross-linked in glutaraldehyde (GA) vapor from the 25% EtOH solution overnight in an airtight chamber.

The 3D printed sacrificial templates were produced using Allevi 1 3D printer with an STL file of the digital model and the 3D printed sodium alginate meshes had predesigned patterns.^{57,58} Briefly, the sodium alginate was directly deposited on a cryogenic substrate, and the resulting sodium alginate mesh was cross-linked in a cold CaCl_2 bath (2.5%) for 10 min and then stored in DI water until further use.

Four types of nanofiber aerogels were generated, but the major focus was on the aerogels with precision macrochannels for future use. The procedure for generating the PCL/gelatin nanofiber aerogels with precision macrochannels was described in our previous studies.⁵⁸ The cross-linked PCL/gelatin nanofiber mat was cut into short nanofibers using a cryostat. The PCL/gelatin short nanofibers were stored at 4 °C for future use. To prepare the aerogels, the PCL/gelatin short nanofibers were dispersed in deionized (DI) water to form a nanofiber solution with a concentration of 25 mg/mL along with the addition of gelatin at a concentration of 1.25 mg/mL. The solution was homogenized in an ice bath for 20 min and then subjected to an additional 20 min using a homogenizer set at 20% amplitude and 10/20 s ON/OFF cycles. CuHARS was added to the solution during the final 3 min of the homogenization, resulting in a final concentration of 0.01% (w/v) in the solution. The homogeneous mixture was then transferred to a copper ring mold fixed on a metal plate and frozen at –80 °C for 1 h. After the mold was completely frozen, the nanofiber aerogels were transferred to a freeze-dryer and subject to lyophilization for 24 h. The aerogels were subsequently cross-linked with GA vapor for 12 h in a closed chamber containing 25% GA in EtOH. The cross-linked aerogels were immersed in a 3 mg/mL solution of alginate lyase in 1 \times PBS. They were then placed in a shaker and incubated at 37 °C for 3 h, during which the alginate templates were dissolved. This step not only removed the excess GA used but also included a final wash with Tris HCl buffer. Subsequently, the aerogels were sterilized using 70% EtOH before being utilized in experiments.

2.5. Structural Morphology of CuHARS-Embedded PCL/Gelatin Nanofiber Aerogels. The morphologies of the aerogels, both with and without CuHARS and macrochannels, were examined using SEM. The CuHARS-embedded aerogels were also examined under an energy-dispersive spectrometer (EDS) to examine the distribution of the CuHARS in the polymeric scaffolds. In brief, the aerogels were frozen in DI water, and then horizontally sectioned using a cryostat. The

sections were subsequently freeze-dried to remove moisture before being sputter-coated with an Au–Pd target in an argon atmosphere at a peak current of 15 A for 5 min. The sputter-coated samples were then imaged using SEM with an accelerating voltage of 15–20 kV.

2.6. Degradation of CuHARS in Passive Cell Culture. The degradation of CuHARS was assessed under passive biological conditions. A 24-well cell culture plate was employed, with 2 mL of HMEC1 media added to 9 wells and 2 mL of 1 × DPBS to another set of 9 wells. CuHARS, with a stock concentration of 5 mg/mL, underwent 20 min of sonication in a Branson 1500 sonicator within a 1.5 mL Eppendorf tube. Another stock solution of CuHARS, also with a concentration of 5 mg/mL, was maintained without sonication. Based on our previous study, we observed approximately 95% degradation of CuHARS in microglia, astrocytes, and PC12 media over a 28-day period.¹² Sonication of CuHARS resulted in lengths of around 3–6 μm as they broke into smaller sections. This enhanced the surface area of interaction, leading to structures resembling those embedded in the scaffolds. Sonicated and nonsonicated CUHARS, both at a concentration of 20 μg/mL, were added to respective wells containing DPBS and HMEC1 media. The culture plate was then placed in an incubator at 37 °C with 5% CO₂. Images were captured using a Leica DMI6000B optical microscope at predefined coordinates within the wells on days 0, 1, 2, 3, 5, 7, 10, 14, 21, and 28 after adding the sonicated and nonsonicated CuHARS.

2.7. Quantification of Cu²⁺ Released Over Time. The release of Cu²⁺ from sonicated CuHARS, both individually and from CuHARS embedded PCL/gelatin nanofiber aerogels in HMEC1 medium, was quantified using ICP-MS. The control group consisted of HMEC1 medium alone. This assessment is crucial since Cu²⁺ plays a pivotal role in initial antimicrobial activity, angiogenesis promotion, and serves as an active indicator of the novel CuHARS's biological degradation. For the experimental setup, six-well cell culture plates were utilized, each containing 6 mL of HMEC1 medium. CuHARS embedded PCL/Gelatin nanofiber aerogels were added to the HMEC1 medium to achieve a final concentration of 10 μg/mL of CuHARS in the HMEC1 media. The plates were then incubated at 37 °C with 5% CO₂ for 28 days. Sampling was performed on days 1, 3, 5, 7, 14, 21, and 28 after CuHARS and aerogel addition. From each set of wells—HMEC1 media, CuHARS 10 μg/mL in HMEC1 media, and CuHARS embedded PCL/gelatin nanofiber aerogels in HMEC1 media, 1 mL of HMEC1 media was collected. To isolate and determine Cu²⁺ concentration using ICP-MS, 1 mL of HMEC1 was mixed with 1 mL of concentrated HNO₃ and 0.5 mL H₂O₂ in polypropylene tubes. The mixture was digested at 60 °C for 2 h, followed by dilution with 2.5 mL of ultrapure water. The resulting solutions were centrifuged at 2000 rpm for 5 min, and the supernatant was dried on a hot plate at 80 °C. The dried residue was then redispersed in a matrix containing 10 ppb Tb for subsequent ICP-MS analysis. ICP-MS analysis was conducted using the PerkinElmer NexION 300Q at the UNMC core facility. Data were collected and provided by the UNMC core facility for further analysis. Calibration standards of 200, 100, 50, 25, 12.5, and 6.25 ppb Cu²⁺ were used. The experiment aimed to determine the release of Cu²⁺ from CuHARS-embedded nanofiber aerogels over 28 days, providing insights into the availability of Cu²⁺ at different time points.

2.8. Synthesis of CysNO and Catalytic Production of NO Using CuHARS. The synthesis of nitric oxide from its precursor, S-nitrosocysteine (CysNO), was assessed using CuHARS. Freshly prepared CysNO was employed for each experiment due to its rapid decomposition upon temperature change. CysNO was synthesized by combining 17.56 mg (0.1 mmol) of cysteine with 12 μL (0.1 mmol) of *tert*-butylnitrite in 1 mL of sterile water. This mixture was kept on ice while continuously shaking for 30 min, following the procedure outlined by Ryan and Reynolds.⁵⁹ The resulting CysNO stock solution is at a concentration of 0.1 M.

2.9. In Vitro Testing for NO Production. The catalytic decomposition of CysNO to generate NO under passive biological conditions was evaluated at concentrations relevant to the biological environment, specifically in the HMEC1 medium. This assessment was conducted using CuHARS and CuHARS embedded within aerogels, exploring various CuHARS and CysNO concentrations. Given that the desired NO concentration in areas of inflammation or wounds is approximately 8 μM, CysNO concentrations of 10, 25, and 50 μM were tested. These tests were carried out in the presence of CuHARS (10 μg/mL) and aerogels containing 4, 8, and 20 μg of CuHARS per 1 mL of HMEC1 media, respectively. To achieve these concentrations, the stock solution of 0.1 M CysNO was diluted with HMEC1 medium accordingly. The goal was to examine how the concentration of endogenous biomimicking NO donor, CysNO, and the catalyst, CuHARS, impacted the production of NO. The quantification of generated NO was achieved using the Thermo Fisher Scientific Greiss assay kit. This was performed following the protocol provided by the company, utilizing a plate reader (Biotek Synergy H1) set at a wavelength of 548 nm.

After achieving the target NO concentration of approximately 8–10 μM, the subsequent experiment focused on assessing the reusability of CuHARS in the NO catalysis process. To carry this out, 10 μg of CuHARS alone and aerogels containing 10 μg of CuHARS were introduced into cell culture wells, each containing 1 mL of HMEC1 media. The catalytic generation of NO was determined using the Greiss assay after 3 h of incubation at 37 °C with 5% CO₂. This was done following the addition of CysNO for 5 consecutive treatments of HMEC1 media, each with 10 μM CysNO. Data points for NO generation were recorded on days 1, 3, and 5. In a previous study, we demonstrated the reusability of 4% (w/w) CuHARS embedded in cellulose films for NO catalysis, but the fresh CysNO was added every 15 min.⁴⁵ In this current study, the reusability of CuHARS and its NO generation capacity were evaluated over a 5-day period within a physiological microenvironment.

2.10. Bactericidal Effect of CuHARS-Embedded PCL/Gelatin Nanofiber Aerogels. Our previous research focused on investigating the bactericidal effect of NO on *E. coli* and *S. epidermidis*.⁴⁵ However, this examination was conducted in a noncontact manner within a bioreactor. In that study, CuHARS acted as a catalyst for NO generation, with the gaseous form of NO applied to bacteria to observe the suppression of bacterial colonies, demonstrating bactericidal effect for a 24 h period.⁴⁵ In this study, we explored the synergistic effect of CuHARS and NO on MRSA. A single bacterial colony of MRSA was cultured by inoculating loops and incubating them at 37 °C and 200 rpm in liquid LB medium overnight. Subsequently, 10 μL of bacterial culture was added to 2 mL of fresh LB and further incubated for about

2 h. The resulting cultures were centrifuged, washed with PBS twice, and then resuspended. Bacteria were diluted to a concentration of 10^7 CFU/mL in PBS. For the testing, six 15 mL polypropylene tubes were prepared, each containing 2 mL of PBS along with MRSA USA300 (10^7 CFU/mL). The materials under investigation included: CysNO (10 μ M/mL), CuHARS (10 μ g/mL), CuHARS (10 μ M/mL) + CysNO (10 μ M/mL), PCL/Gelatin aerogels + CysNO (10 μ M/mL), CuHARS embedded aerogels (10 μ g/mL) + CysNO (10 μ M/mL). The goal was to assess MRSA viability over 4 h using the Invitrogen Bacterial Live/Dead assay, following the company's protocol. For the experimental procedure, CysNO with a total concentration of 10 μ M/mL was added to the tubes with MRSA first, followed by the addition of CuHARS (10 μ g/mL) or aerogels (containing 10 μ g/mL of CuHARS). The tubes were then incubated at 37 °C for 4 h. After this incubation period, the Thermo Fisher Scientific bacteria Live/Dead assay kit was used according to the company's instructions. For confocal imaging, 20 μ L of the assay solution was placed on a glass slide, covered with a glass coverslip, and imaged using Zeiss LSM 800 with an Airyscan microscope in the UNMC confocal core facility. Percentages of dead bacterial cells were determined relative to the total bacterial cells within each field. Furthermore, the treated MRSA from the previous experiment was incubated on agar plates to observe regrowth and colony formation. Colonies were counted under various experimental conditions after 24 h to assess any changes in MRSA colony formation.

2.11. Formation of Lumen and Viability Analysis of Human Microvascular Endothelial Cells (HMEC1). For *in vitro* cell studies, human microvascular endothelial cells 1 (HMEC1) were used. These cells were generously provided by Dr. Rakesh Singh at UNMC. HMEC1 cells were cultured in RPMI 1640 medium (ThermoFisher Scientific), supplemented with 10% fetal bovine serum and 1% penicillin–streptomycin. Upon reaching confluency, the cells were rinsed with DPBS and then treated with trypsin-EDTA (0.25%) for 5 min to facilitate cell detachment from the culture plate. Following this, the cells were centrifuged at 1000 rpm for 5 min to collect the cell pellet. The supernatant was removed, and the cell pellet was resuspended in fresh media before being plated for further use.

The tube assay was performed on Cultrex BME low-growth factor-coated coverslips (R&D systems). On the assay day, 80,000 cells were seeded onto the coverslips and allowed to adhere for 6 h. Following this initial attachment period, the adhered cells were exposed to various conditions: control, 10 μ M/mL CysNO, 10 μ g/mL CuSO₄, 10 μ M/mL CysNO + 10 μ g/mL CuSO₄, 10 μ g/mL CuHARS, and 10 μ M/mL CysNO + 10 μ g/mL CuHARS. After an additional 18 h of incubation at 37 °C with 5% CO₂, tube formation was assessed and compared between differentiation treatment conditions and untreated control conditions. The cells were fixed using 4% paraformaldehyde (PFA) and stained with calcein (ThermoFisher Scientific). Subsequently, visualization was conducted using the Zeiss LSM 800 with Airyscan microscope located within the UNMC confocal core facility. Images were acquired, analyzed, and processed using the Zeiss Zen 2010 software. Quantification of all confocal data was performed using ImageJ software, and graphical representations were generated using GraphPad Prism software.

Approximately 1.0×10^3 HMEC1 cells were seeded per well in a 24-well plate and allowed to adhere for 6 h. The cells were

subjected to various treatment conditions, including control, 10 μ M/mL CysNO, 10 μ g/mL CuSO₄, 10 μ M/mL CysNO + 10 μ g/mL CuHARS, 10 μ M/mL CysNO + PCL/gelatin aerogels, and 10 μ M/mL CysNO + PCL/gelatin aerogels containing 10 μ g/mL CuHARS. To assess cell viability, a CCK-8 assay (Dojindo Lab) was conducted at 24 and 48 h, following the protocols provided by the company. The absorbance was measured using Biotek Synergy H1 plate reader at a wavelength of 450 nm. The data were analyzed by normalizing the viability of the 24 h control group to 100% and was presented in the form of a bar graph.

2.12. Transwell Migration of HMEC1 and VEGF Quantification. Five $\times 10^4$ HMEC1 cells per insert of a 24-well transwell plate were plated and allowed to attach for 4 h. In the lower chamber of the well, various test conditions, including control, 10 μ M/mL CysNO, 10 μ g/mL CuSO₄, 10 μ M/mL CysNO + 10 μ g/mL CuSO₄, 10 μ g/mL CuHARS, and 10 μ M/mL CysNO + 10 μ g/mL CuHARS, were added to establish a gradient across the membrane. The media in the inset were removed, and the cells were allowed to migrate toward the gradient for 24 h. Media from the lower chamber of the well were collected to assess VEGF levels. The migrated cells were gently washed with $1 \times$ DPBS and fixed using formalin for 15 min. Formalin was then removed, and the cells were washed with $1 \times$ DPBS. Subsequently, 1 mL of Crystal violet dye was added to the cells and stained for 20 min. The dye was thoroughly washed with distilled water, and images were captured using a Leica DMI6000B optical microscope. The images were analyzed to calculate and compare the relative percentage of migration between the control and the test conditions. The data obtained were presented as a bar graph, and statistical significance was determined from 3 independent experiments. The VEGF levels were quantified by ELISA assay kit from Abcam following the manufacturer's protocol, and the data were calculated and represented as a bar graph.

2.13. Angiogenic Gene Expression Analysis by PCR. 0.3×10^6 HMEC1 cells were plated in each well of a six-well plate and allowed to settle for 4 h. Various test conditions, including control, 10 μ M/mL CysNO, 10 μ g/mL CuSO₄, 10 μ M/mL CysNO + 10 μ g/mL CuSO₄, 10 μ g/mL CuHARS, and 10 μ M/mL CysNO + 10 μ g/mL CuHARS, were added to the cells and incubated for 48 h. The cells were washed with $1 \times$ DPBS twice and 1 mL of trizol (ThermoFisher Scientific, CA) was added to each well to collect cell lysate. Phase separation was achieved by adding chloroform, followed by RNA precipitation with ethanol. The resulting pellet was air-dried and resuspended in RNase- DNase-free distilled water. The RNA concentration was determined using a Nanodrop spectrophotometer (ThermoFisher Scientific). One milligram of RNA was used to generate cDNA following the protocol of the Transcriptor First strand cDNA synthesis kit (Roche Diagnostics Corporation). Fifty nanograms of cDNA were used for real-time PCR using the SYBR green detection system. The reactions were conducted using an ABI 7500 instrument located in the Department of Surgery at UNMC. Data analysis involved normalization with 36B4, measured under the same conditions, using the $2^{-\Delta\Delta CT}$ method. The list of primers used is as follows.

VEGF Forward-5'-CCC ACT GAG GAG TCC AAC AT-3'
Reverse- 5'-AAA TGC TTT CTC CGC TCT GA-3'
VEGF-R1 Forward-5'-CATGAGGATGAGAGCTCCT-
GAG-3'

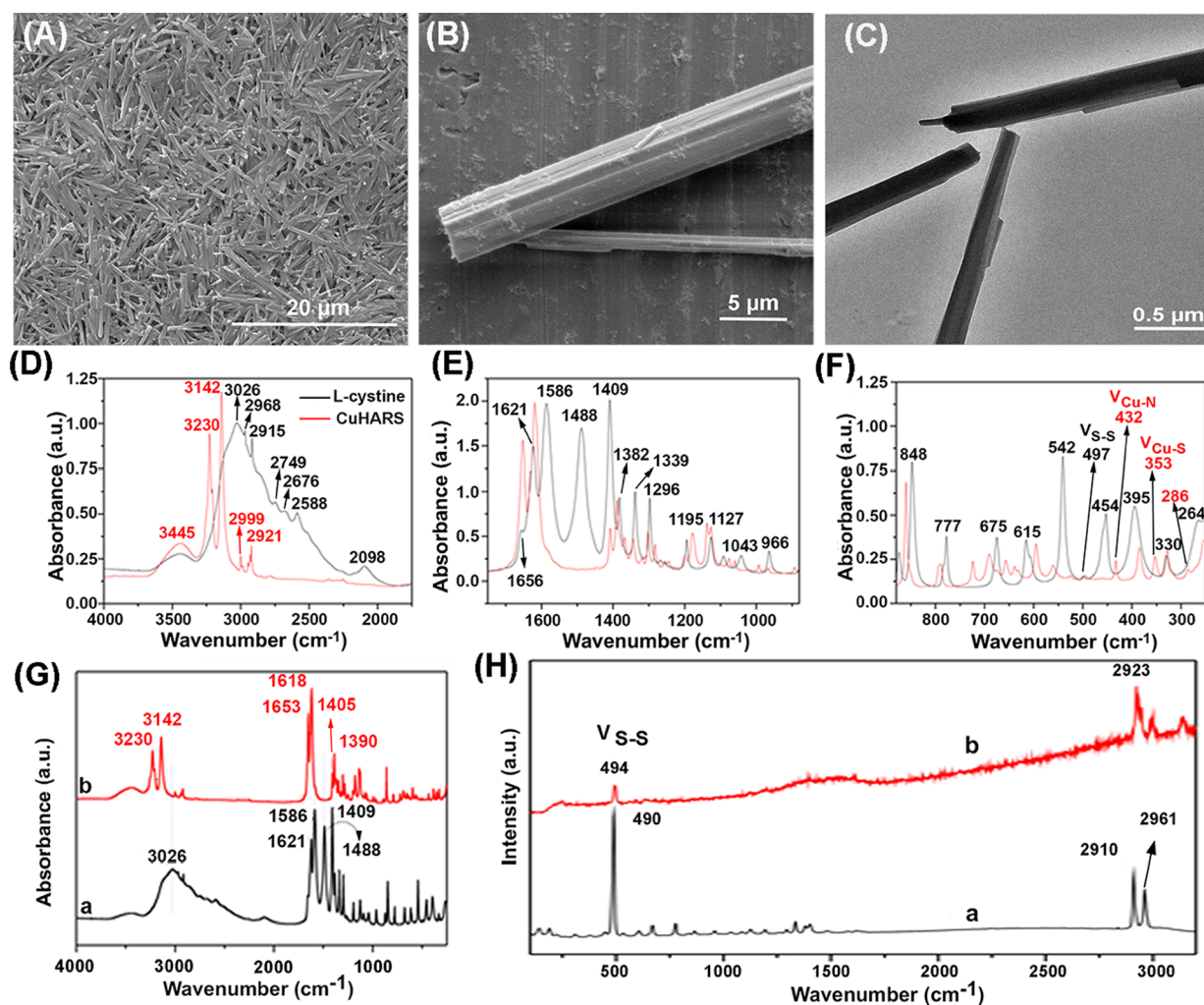


Figure 1. Characterizations of CuHARS. (A) SEM image of CuHARS. (B) Higher magnification of (A). (C) TEM image of CuHARS showing the solid internal structure. (D) FTIR spectra in the range of 4000–1750 cm^{-1} . (E) FTIR spectra in the range of 1750–900 cm^{-1} . (F) FTIR spectra in the range of 900–250 cm^{-1} . (G) FTIR spectra in the range of 4000–250 cm^{-1} of (a) L-cystine and (b) CuHARS. (H) Raman spectra in the range of 3200–100 cm^{-1} of (a) L-cystine and (b) CuHARS. The spectra were normalized based on the most intense band in each case.

Reverse-5'-AGCCAACAGAGTGCTGCTGTC-3'
 VEGF-R2 Forward-5'-GCA ATC CCT GTG GAT CTG
 AA-3'

Reverse-5'-ACT CCA TGC CCT TAG CCA CT-3'
 BFGF Forward-5'-CCG TTA CCT GGC TAT GAA GG-3'
 Reverse-5'-ACT GCC CAG TTC GTT TCA GT-3'
 TGF- β Forward-5'-CATGGAGCTGGTGAAACGGA-3'
 Reverse-5'-GGCGAGCCTTAGTTTGGACA-3'
 ANG1 Forward-5'-GAA GGG AAC CGA GCC TAT TC-3'
 Reverse-5'- GCT CTG TTT TCC TGC TGT CC-3'
 36B4 Forward-5'-ATG CAG CAG ATC CGC ATG T-3'
 Reverse-5'-TCA TGG TGT TCT TGC CCA TCA -3'

2.14. Statistical Analysis. Statistical analysis was conducted using Graphpad Prism software from Graphpad Software Inc., located in San Diego, CA. The results were presented as means \pm standard errors ($n = 3$). Statistical significance was determined using RM two-way ANOVA with Geisoor-Greenhouse correction and Tukey's multiple comparison tests (applied for $n = 3$) as well as Brown-Forsythe and Welch Anova ($n = 1$). In the Figures illustrating the degradation of CuHARS, the release of Cu^{2+} , reusability of CuHARS, bactericidal effect, lumen formation, cell viability, cell migration, VEGF ELISA assay and angiogenic gene

profiling through PCR analysis, statistical significance levels were represented as follows: ns ($p > 0.05$), * ($p \leq 0.05$), # ($p \leq 0.01$), and ∞ ($p \leq 0.001$).

3. RESULTS AND DISCUSSION

3.1. Characterization of CuHARS. The complexation of Cu^{2+} with L-cystine results in a blue crystalline material exhibiting a fibrous morphology characterized by a high aspect ratio. This can be observed in the scanning electron microscopy (SEM) images (Figure 1A). From diluted solutions, crystals could grow to lengths of up to approximately 150 μm with diameters ranging from 5 μm down to as small as 100 nm, as observed in the thinnest fibers. When examined under the transmission electron microscope (TEM), these fibers exhibited a solid structure throughout (Figure 1C), validating the uniform integration of both metallic and organic constituents in the biohybrid structures. A prior investigation into CuHARS suspensions reported a zeta potential range of -28 to -33 mV, underscoring the overall negative charge carried by these fibers.^{10,56} To pinpoint the surface charge of CuHARS fibers, titration to the point of zero charges was conducted using the cationic polymer polyDACMAC, yielding a value of 4.8 mequiv of negative charges per 100 g of material.

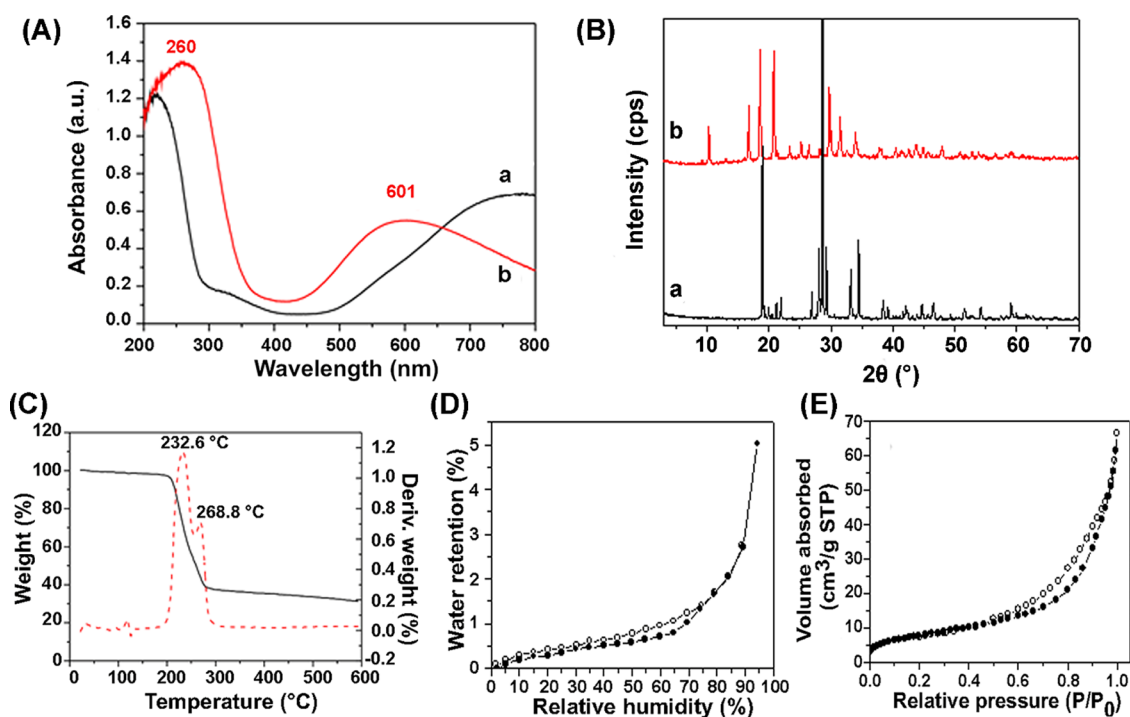


Figure 2. Characterizations of CuHARS. (A) UV–vis spectra of (a) CuSO₄·5H₂O and (b) CuHARS. (B) Powder X-ray diffraction patterns of (a) L-cystine and (b) CuHARS. (C) TG and DTG curves obtained from the thermal analysis of CuHARS, (D) water, and (E) N₂ adsorption/desorption isotherms of CuHARS measured at 25 °C and −196 °C. Solid circle: adsorption; hollow circle: desorption.

This negative charge facilitated the electrostatic adsorption of positively charged polymers such as polyallylamine, which was recently employed to furnish the fibers with a coating containing amino groups. This coating served to aid the covalent attachment of the fibers to 2,2,6,6-tetramethylpiperidine-1-oxyl (TEMPO)-oxidized cellulose.⁴⁵

The quantity of L-cystine assembled with copper ions was assessed through CHNS chemical analysis, resulting in the following outcomes: %C: 23.63; %H: 3.48%; %N: 9.06; %S: 20.72. Consequently, 79% of the total mass within CuHARS consists of L-cystine, while 21% accounts for copper ions. These findings indicate that 0.33 mol corresponds to each component, thereby confirming a 1:1 stoichiometry, consistent with preliminary investigations of this material.⁷ EDS analysis previously established that these elements, alongside oxygen, constitute the sole constituents of the CuHARS material. Upon analyzing pristine L-cystine, values of 30.18%C, 5.02%H, 11.65%N, and 26.58%S, were obtained. This consistent C/S ratio of 0.88 affirms that all the sulfur content in the hybrid material originates from L-cystine, precluding any contribution from residual components such as sulfate ions.

Figure 1D,E show the Fourier transform infrared (FTIR) spectrum of CuHARS, indicating distinct alterations in the characteristic vibration bands of carboxylic and amino groups compared to the cystine spectrum. The stretching vibration bands associated with amino groups in L-cystine, initially located at 3026 cm^{−1} as a broadband (asymmetric ν_{N–H} in NH₃⁺), alongside minor signals ranging from 2750 to 2550 cm^{−1} and an additional peak at 2090 cm^{−1} attributed to the symmetric N–H vibration in NH₃⁺, exhibited a shifted to higher wavenumber values in the CuHARS spectrum. Notably, this shift manifested as two narrow bands at 3230 and 3142 cm^{−1}.⁶⁰ This phenomenon can be attributed to the coordination of copper ions, which form the metal–organic

material. Similarly, the deformation vibration bands observed at 1621 cm^{−1} (asymmetric δNH₃⁺) and 1488 cm^{−1} (symmetric δNH₃⁺) exhibit pronounced susceptibility to metal coordination. The former experiences a shift toward 1653 cm^{−1}, while the robust band at 1488 cm^{−1} appears to manifest at 1408 cm^{−1}, albeit with diminished intensity. This alteration is a consequence of the coordination and subsequent attenuation of the N–H bond, distinct from the free NH₃⁺, as illustrated in Figure 1E.⁶⁰ A similar phenomenon was evident in the bands associated with the carboxylic groups. The band situated at 1586 cm^{−1} (asymmetric C=O stretching) undergoes a shift to 1618 cm^{−1}, while the band at 1409 cm^{−1} (symmetric C–O stretching) likely shifts to a lower frequency around 1390 cm^{−1}, in line with reports on coordination complexes.⁶⁰ Various bands emerging below 550 cm^{−1} could be attributed to the Cu–O and Cu–N bonds established within the CuHARS material (Figure 1F). These observations substantiate the coordination of L-cystine to Cu²⁺ through its amino and carboxylic groups, forming a metal–organic complex. This finding aligns with other studies that detail the fabrication of Cu²⁺ doped crystals of different amino acids, suggesting an arrangement where Cu²⁺ occupies the core of a square-planar geometry constituted by two carboxyl groups and two amino groups.⁶¹

Although the stretching vibration band attributed to the disulfide bond is weak in the IR and challenging to detect, it becomes discernible at 497 cm^{−1} in both the spectra of L-cystine and CuHARS, albeit with very low intensity (Figure 1G). This presence suggests that the bond remains intact even after the coordination of copper(II) ions. Further validation is offered by Raman spectroscopy, where the disulfide bond generates a robust signal. The Raman spectrum of L-cystine (Figure 1H) features certain vibrational bands mirrored in the infrared (IR) spectrum, along with a prominent signal at 490

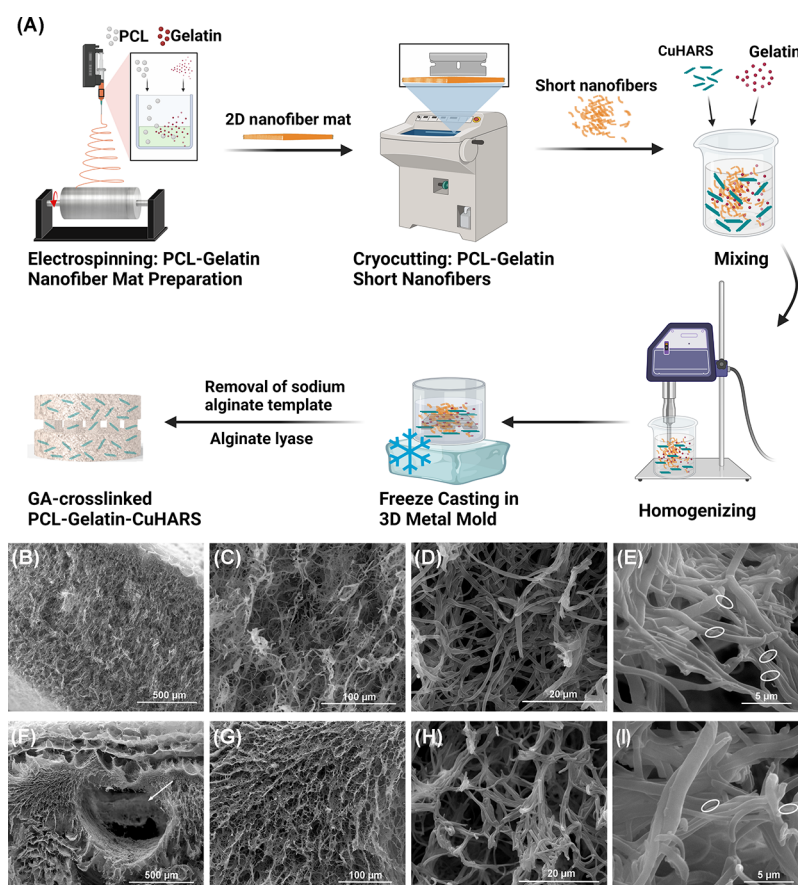


Figure 3. Fabrication and morphological characterization of CuHARS-embedded PCL/gelatin nanofiber aerogels. (A) Schematic illustrating the synthesis of CuHARS-embedded PCL/gelatin nanofiber aerogels with and without patterned channels. (B–E) SEM images at different magnifications showing cross sections of the CuHARS-embedded PCL/gelatin nanofiber aerogels without patterned channels. (F–I) SEM images at different magnifications showing cross sections of the CuHARS-embedded PCL/gelatin nanofiber aerogels with patterned channels. White circles indicate the CuHARS attached to the PCL/gelatin nanofibers. White arrows in (F) indicate the channel formed after dissolving 3D-printed calcium alginate templates.

cm^{-1} attributable to the stretching vibration of the S–S bond. Despite the challenges posed by CuHARS instability and later light absorption, the Raman spectrum of CuHARS managed to capture this disulfide backbone related signal (Figure 1H). This outcome underscores the fact that the disulfide bond remains unbroken within the metal–organic material.⁵⁶ Moreover, the FTIR results, along with Raman findings, imply that the metal ions are likely bonded through the amine and carboxylic groups within the amino acid dimer. This alignment concurs with analogous coordination complex studies involving Zn(II) and cystine or Cu(II) and bis(3-sulfopropyl)-disulfide (SPS).^{62,63} The presence of copper and sulfur as exclusive structural components in CuHARS is validated through energy-dispersive spectroscopy (EDS), as illustrated in Figure S1.

The UV–vis characterization of CuHARS in the solid state reinforces the earlier findings from FTIR and Raman analyses. The UV–vis spectrum of CuHARS reveals two distinct bands at 261 and 601 nm (Figure 2A). The former corresponds to the $n-\pi^*$ characteristic band associated with the C=O bond in L-cystine, while the latter, positioned in the visible range, is attributed to electronic d–d transitions.⁶⁴ In hydrated Cu(II) ions, a pale blue hue emerges due to absorption around 775 nm. When coordinated with L-cystine, this absorption shifts to around 600 nm, reflecting an increased gap between the energy

levels of the d orbitals.⁶⁵ This shift signifies the augmented stability of the resulting complex.

Figure 2B shows X-ray diffraction (XRD) patterns of L-cystine and CuHARS, indicating their crystallinity. Two polymorphs of L-cystine are known, a tetragonal phase ($P4_1$) and a hexagonal phase ($P6_122$).^{66,67} The coordination of copper ions with L-cystine within CuHARS similarly yields a crystalline structure. Interestingly, the presence of metal atoms appears to induce an expansion in the cell dimensions. This effect is implied by the emergence of new reflections at lower $2-\theta$ angles, indicative of larger interatomic distance.

Thermogravimetric analysis was employed to delineate the distinct stages of CuHARS decomposition. A desiccated CuHARS sample underwent gradual degradation within a nitrogen gas environment spanning from 0 and 600 °C. Minor peaks at approximately 90–120 °C in the thermogravimetric analysis (TGA) (Figure 2C) correspond to water loss, albeit minimal in this sample, constituting less than 1%. CuHARS exhibited stability until 200 °C, beyond which weight ensued at higher temperatures, ranging from 200 and 300 °C. This weight loss can be attributed to the melting and thermal decomposition of L-cystine, exhibiting two distinct stages at 232.6 and 268.8 °C. These processes collectively account for around 30% of the total weight loss, aligning with the complete decomposition of CuHARS' organic content. A comparison to prior thermogravimetric (TG) curves of pristine L-cystine,

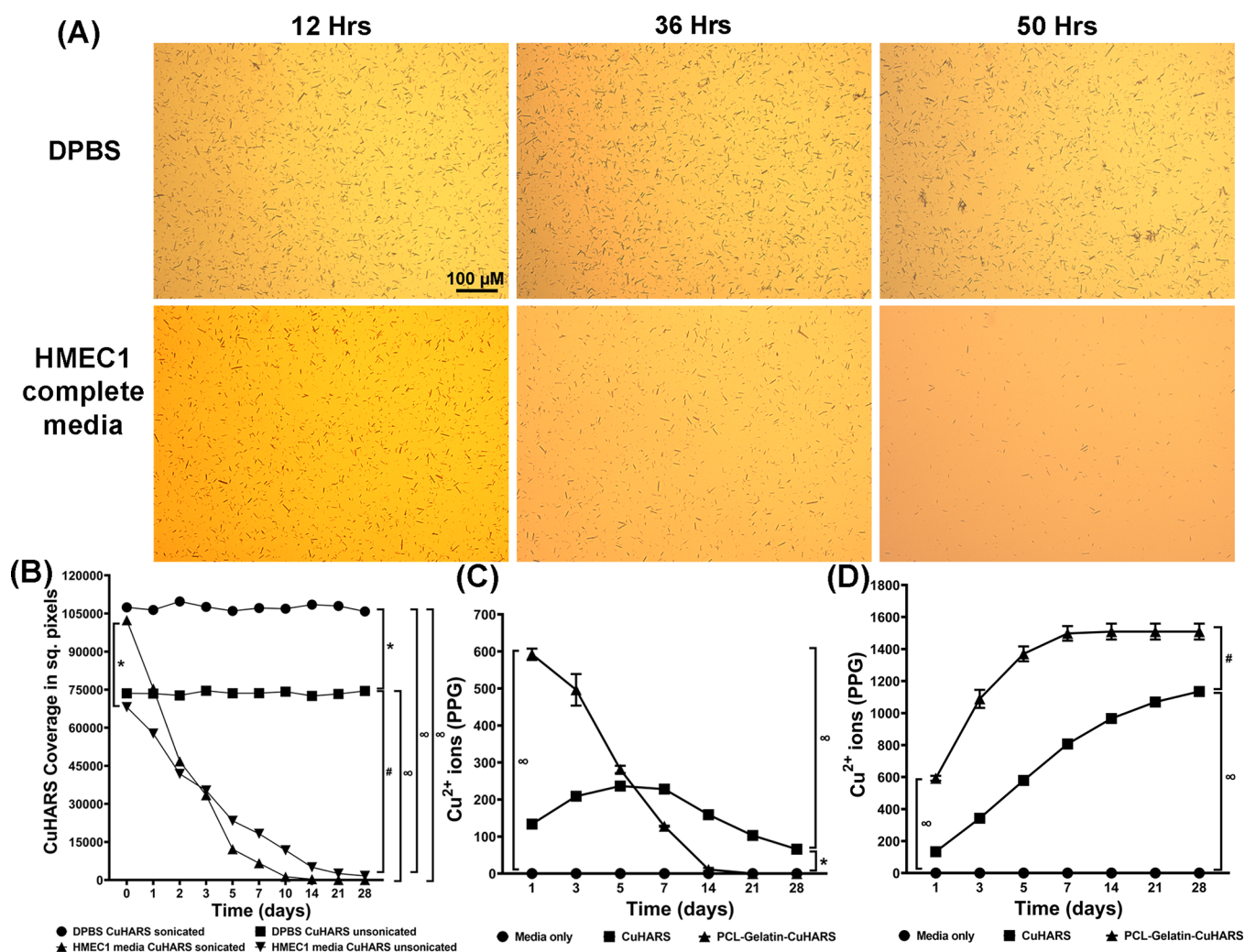


Figure 4. CuHARS degradation and Cu²⁺ release. (A) Microscopic images captured by maintaining a fixed well coordinates and presented to evaluate degradation of sonicated CuHARS over 28 days in DPBS and HMEC1 media incubated at 37 °C in the presence of 0.5% CO₂. (B) CuHARS coverage in DPBS and HMEC1 media with and without sonication. (C) Cu²⁺ release from CuHARS embedded in PCL/gelatin nanofiber aerogels and CuHARS at each time point. (D) Cu²⁺ cumulative release from CuHARS embedded in PCL/gelatin nanofiber aerogels and CuHARS for 28 days. The experiment was conducted three times ($n = 3$), and the p values were calculated and denoted as ns ($p > 0.05$), * ($p \leq 0.05$), # ($p \leq 0.01$), and ∞ ($p \leq 0.001$).

which displays two mass losses at lower temperatures (203.9 and 239.9 °C), suggests that the coordination with copper(II) ions increases the thermal stability of the amino acid within the hybrid material by about 30 °C.⁶⁸

Gravimetric water sorption analysis revealed an exceedingly low water content in CuHARS, estimated at around 0.65%, corroborating the TG findings. The initial section of the water sorption isotherm (Figure 2) at low relative humidity (RH) levels, following the Langmuir adsorption model, demonstrated a maximum water uptake of around 0.3%, adsorbed as a monolayer on the external surface. This outcome underscores the remarkably limited availability of adsorption sites within this material. With escalating RH, the CuHARS fibers could adsorb a mere 5% of water at most, likely attributed to water cluster adsorption at the highest RH values. Further analysis of this water sorption isotherm unveiled a scant Brunauer–Emmett–Teller (BET) specific surface area of around 32 m²/g, reaffirming the absence of porosity. These results found corroboration in N₂ adsorption/desorption analysis. The resultant isotherm (Figure 2D,E) emulates a type II isotherm, characteristic of dense materials. The BET-specific surface area

registered at 28 m²/g, while the t-plot method concurred with the lack of microporosity within this sample, closely aligning with the water sorption isotherm analysis.

3.2. Characterization of CuHARS-Embedded Poly(ϵ -caprolactone) (PCL)/gelatin Nanofiber Aerogels. Given the potential applications of CuHARS in NO catalysis, angiogenesis, and antibacterial effects, embedding CuHARS at a concentration of 0.1% w/w within PCL/gelatin nanofiber aerogels was undertaken. The schematic depiction of the process for crafting channeled nanofiber aerogels embedded with CuHARS is shown in Figure 3A. The SEM images in Figure 3 show the CuHARS-embedded PCL/gelatin nanofiber aerogels with and without microchannels. In Figure 3B–E, vertical cross sections of the aerogels without microchannels are presented at different magnifications (100×, 400×, 1000×, and 10000×) captured via SEM. The aerogels devoid of channels lack adequate pore size to facilitate the infiltration of migrating keratinocytes or endothelial cells, thereby restricting the development of granular and vascular tissues within the aerogels. Consequently, cells tend to remain preliminarily at the aerogel periphery. Attachment sites of CuHARS within the

cross-linked gelatinous aerogels are shown in Figure 3E, marked by white ellipses. The EDS analysis on the CuHARS-embedded PCL/gelatin nanofiber aerogels shows the homogeneous distribution of CuHARS in the PCL/gelatin nanofibers aerogels as shown in Figure S2. To encourage cellular migration and accelerate wound regeneration with the aerogels, sacrificial calcium alginate templates were used during the preparation of CuHARS-embedded PCL/gelatin nanofiber aerogels with patterned macrochannels. This strategy enabled the construction of an internally structured framework of microchannels, with diameters approximating 300–500 μm , conducive to the migration of various cell types, including keratinocytes, human microvascular endothelial cells and human dermal fibroblasts (HDFs). This architectural design preserves a successful extracellular biomimetic nanofibrous architecture. SEM images of the vertical cross-section of the aerogels with microchannels, captured at varying magnifications (100 \times , 400 \times , 1000 \times , and 10000 \times) are shown in Figure 3F–I. The efficacy of similar aerogel types has been demonstrated in prior studies.^{58,69} However, the present study delves into the effect of the gradual release of Cu^{2+} from CuHARS embedded within the aerogels. This investigation explores their roles in fostering angiogenesis and delivering a short-term burst of antibacterial effect.

3.3. Degradation of CuHARS and Release of Cu^{2+} from the Aerogels. The biodegradability of CuHARS has previously been addressed in a preceding study, where the degradation of CuHARS was elucidated under passive biological conditions.¹² In this context, the degradation of CuHARS was observed to reach up to 95% within diverse brain cell culture media over 18 days, incubated at 37 $^{\circ}\text{C}$ with 5% CO_2 . Given this, it became imperative to examine the degradation profile of sonicated CuHARS under analogous conditions upon exposure to human endothelial cell media. Typically, sonicated CuHARS display lengths of approximately 3–6 μm , compared to the nonsonicated CuHARS spanning 5–150 μm . The reduced length of sonicated CuHARS enhances the overall surface area and the interface available for interaction with any biological medium. The rationale for investigating the degradability of sonicated CuHARS stemmed from their utilization in the form of PCL/gelatin aerogels, wherein ultrasonication is employed to homogenize short nanofibers during fabrication—resulting in CuHARS being broken down to the size of sonicated CuHARS. The degradation characteristics of both sonicated and nonsonicated CuHARS were evaluated in Dulbecco's phosphate-buffered saline (DPBS) and human microvascular endothelial cell line (HMEC1) medium. The degradation process was monitored over 28 days through optical microscopy, with the relative CuHARS coverage area quantified in terms of square pixels. As depicted in Figure 4, a gradual degradation of CuHARS over time was evident. Notably, sonicated CuHARS did not display degradation in DPBS; however, within HMEC1 media, a rapid degradation was observed within the initial 50 h (Figure 4A). By day 14, sonicated CuHARS exhibited complete degradation, whereas nonsonicated CuHARS showed nearly 95% degradation by the same time point. Yet, full degradation for nonsonicated was not attained even by day 28 in HMEC1 medium (Figure 4B). Interestingly, both sonicated and nonsonicated CuHARS exhibited negligible degradation in DPBS (Figures 4A, S3). The relative coverage area of sonicated CuHARS declined from 102 to 0.3 k pixel² from day 0 to day 14, with an initial burst degradation of 88.14% in

the first 5 days. Similarly, the relative coverage area of nonsonicated CuHARS exhibited a reduction from 68 to 5 k pixel² from day 0 to day 14, with an initial degradation of 65.7% in the first 5 days in the HMEC1 medium (Figure 4B). The extended time taken for larger CuHARS to degrade is attributed to their greater size, which consequently reduces the available interfacial surface for interaction with HMEC1 media. The observed degradation of CuHARS under physiological conditions likely results from the presence of the metal-chelating reagents present within the serum of cell culture media. Notably, cell culture medium containing fetal bovine serum encompasses metal-binding proteins, such as ceruloplasmin—a serum ferroxidase capable of binding to copper sources and chelating copper present in CuHARS.^{70,71} Furthermore, the organic component L-cysteine within CuHARS when liberated, acted as an active participant in cellular metabolic activity, thereby contributing to the maintenance of viability in the human microvascular endothelial cells under investigation.

Copper ranks as the third most vital metal in the human body, yet its concentration within a localized region bears a threshold value beyond which it may manifest its toxicity. Ordinarily, copper content in human blood rests around 1 mg/L, while the total copper mass within an adult human body spans 50–129 mg.^{72,73} In this study, the extent of Cu^{2+} release from nonsonicated CuHARS and CuHARS-embedded PCL/gelatin nanofiber aerogels over a 28-day period was quantified via inductively coupled plasma mass spectrometry (ICP-MS) (Figure 4C,D). Notably, the release of Cu^{2+} from CuHARS is directly highest on its degradation dynamics. On day 1, nonsonicated CuHARS yielded a release of 133.6 ± 15.85 ppb Cu^{2+} , which eventually escalated to an overall release of 966.17 ± 10.76 ppb Cu^{2+} by day 14, with an initial release of 51.01% Cu^{2+} during the first 5 days. Conversely, CuHARS embedded within PCL/gelatin nanofiber aerogels commenced with a day 1 release of 592.33 ± 26.4 ppb Cu^{2+} , culminating in a total release of 1509.04 ± 6.82 ppb by day 14, accompanied by an initial release of 90.78% Cu^{2+} within the initial 5 days. This observation indicated a complete 100% release of Cu^{2+} from the PCL/gelatin aerogels on day 20 as demonstrated in Figure 4C since the Cu^{2+} ions concentration reached zero. The accelerated Cu^{2+} release from the nanofiber aerogels can be attributed to the state of sonication that the CuHARS within aerogels undergo. This was in line with the findings of the degradation comparison between sonicated and nonsonicated CuHARS in HMEC1 media, where sonicated CuHARS underwent complete degradation within the initial 14 days. The smaller the size of CuHARS, the faster it degrades because of the increase in the interacting surface area of the material. Figure 4D presents the day-by-day release of Cu^{2+} on days 1, 2, 3, 4, 5, 7, 14, 21, and 28, both from nonsonicated CuHARS and CuHARS-embedded PCL/gelatin aerogels. The release of Cu^{2+} from CuHARS plays a pivotal role in catalyzing RSNO to NO and significantly contributes to the initial stages of angiogenesis.

3.4. Catalytic Production of NO in the Presence of CuHARS-Embedded PCL/gelatin Nanofiber Aerogels. In a previous study conducted by Darder et al., it was estimated that 4% w/w CuHARS within their cellulose films released around 0.44 ± 0.01 nmol/s of Cu^{2+} , generating sufficient NO to exhibit antimicrobial activity against *Escherichia coli* (*E. coli*) and *Staphylococcus epidermidis* (*S. epidermidis*). However, the delivery method utilized in that study was noncontact,

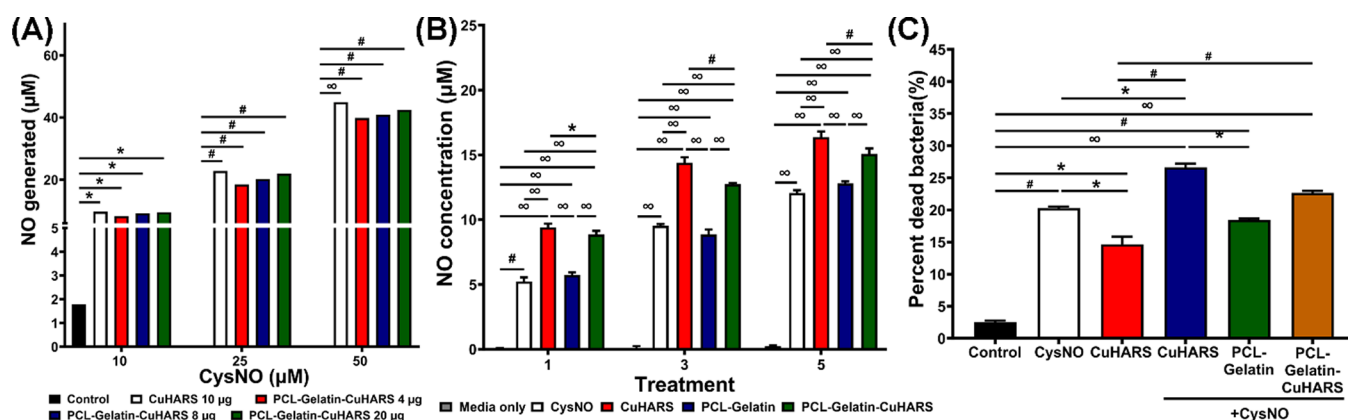


Figure 5. NO production and antibacterial activity. (A) NO production from 10, 25, and 50 μM of CysNO solutions in the absence and presence of sonicated CuHARS and CuHARS-embedded PCL/gelatin nanofiber aerogels (containing 4, 8, and 20 μg of sonicated CuHARS). (B) NO release from CuHARS-embedded PCL/gelatin nanofiber aerogels (containing 10 μg of CuHARS) after treatment with 10 μM of CysNO every day for 1, 3, and 5 consecutive days. (C) Antibacterial effect of sonicated CuHARS (10 μg) and CuHARS-embedded PCL/gelatin nanofiber aerogels (containing 10 μg of CuHARS) against MRSA USA300 (10^7 CFU/mL) in the presence and absence of CysNO (10 μM /mL) for 4 h. Control: without treatment. $n = 3$ with p values calculated and denoted as ns ($p > 0.05$), * ($p \leq 0.05$), # ($p \leq 0.01$), and ∞ ($p \leq 0.001$).

involving the catalysis of NO by CuHARS.⁴⁵ The concentration of CuHARS used in the study was significantly higher to generate an ample amount of NO which became a potent bactericidal agent over a period of 24 h. The primary goal of this study was to identify an appropriate concentration of CuHARS to be delivered through nanofiber aerogels, which could produce enough amount of Cu^{2+} for both antibacterial activity and the catalysis of NO from RSNO within wound regions while operating in direct contact with the physiological wound environment. Figure 5A illustrates the calibration for delivering 10 μg of sonicated CuHARS, along with 4, 8, and 20 μg of CuHARS embedded individually within nanofiber aerogels. These concentrations were selected in a cytocompatible manner using 10, 25, and 50 μM of CysNO, aiming to understand the corresponding change in NO concentration resulting from the catalytic process. Although CysNO is known to decompose into NO at 37 $^\circ\text{C}$, the presence of Cu^{2+} released from CuHARS degradation within HMEC1 media demonstrated a similar trend of elevated NO release. Given that the typical concentration of RSNOs within wound or inflammation areas could be around ~ 8 μM , the optimization of *in vitro* experimental setup was necessary to gain insights into the alteration of NO levels due to the presence of released Cu^{2+} . The NO generated from 10, 25, and 50 μM CysNO amounted to 1.79, 3.56, and 6.64 μM , respectively. With higher concentrations of CysNO in the HMEC1 medium, the decomposition of CysNO to NO also increased, albeit being considered incomplete. The presence of copper had the potential to enhance NO generation. When 20 μg of sonicated CuHARS were present in 1 mL of HMEC1 medium containing 10 μM CysNO, and 4, 8, and 20 μg of CuHARS were embedded within PCL/gelatin aerogels, the catalyzed NO concentration spiked to 9.68, 8.28, 9.15, and 9.5 μM , respectively, as shown in Figure 5A. Similarly, in HMEC1 media containing 50 μM CysNO, the presence of comparable concentrations of sonicated CuHARS and CuHARS embedded in PCL/gelatin nanofiber aerogels, resulted in concentrations of 44.90, 39.82, 40.87, and 42.45 μM , respectively. These findings support the notion that higher concentrations of free Cu^{2+} effectively enhance the catalytic decomposition of RSNO into NO.

The reusability of CuHARS stands as a crucial parameter, especially since the concentration of CuHARS within nanofiber aerogels for wound use remains fixed, and the variable factor is the continual influx of RSNOs through the bloodstream into the wound site. Gradual degradation must facilitate the progressive catalysis of RSNOs to generate a sustained NO supply. Since the concentration of RSNOs within the wound regions is around 8 μM , CuHARS reusability was assessed using a 10 μM CysNO concentration within HMEC1 medium for the production of elevated NO mimicking normal physiological condition. For consistency, the concentration of both sonicated CuHARS and CuHARS embedded in PCL/gelatin aerogels was set at 10 μg per mL of HMEC1 medium. This range of NO concentrations, such as ~ 7 –15 μM , is sufficient for stimulating angiogenesis and facilitating bactericidal activity, as demonstrated in this research.⁷⁴ The assessment of CuHARS reusability was conducted under passive physiological conditions, where CuHARS acted as an active Cu^{2+} donor for catalyzing NO production over an extended period, crucial for complete vascularization. Comparing the control (10 μM CysNO in HMEC1 medium) with the scenario involving PCL/gelatin aerogels in 10 μM CysNO, the generated NO concentration during the first, third, and fifth treatments with 10 μM CysNO were similar (5.22 ± 0.79 , 9.53 ± 0.51 , and 11.75 ± 0.61 μM , respectively for the control, and 5.71 ± 0.71 , 8.85 ± 0.66 , and 11.79 ± 0.62 μM , respectively for the aerogels). These results clearly indicate the NO amount generated from CysNO decomposition. In contrast, when exposed to 10 μg of sonicated CuHARS or PCL/gelatin aerogels containing 10 μg embedded CuHARS, a notable spike in NO concentrations occurred during the first, third, and fifth treatments on days 1, 3, and 5, respectively. Specifically, 10 μg of sonicated CuHARS yielded 9.41 ± 0.6 , 14.39 ± 0.76 , and 17.36 ± 0.78 μM of NO, while PCL/gelatin aerogels with 10 μg CuHARS resulted in 8.85 ± 0.8 , 12.73 ± 0.61 , and 15.47 ± 0.78 μM of NO during first, third and fifth treatments with 10 μM CysNO, as depicted in Figure 5B. These findings confirm that the increasing concentration of released Cu^{2+} into the HMEC1 medium over the initial 5-day period (Figure 4D) correlates with the heightened catalysis of NO from CysNO. This cascade effect

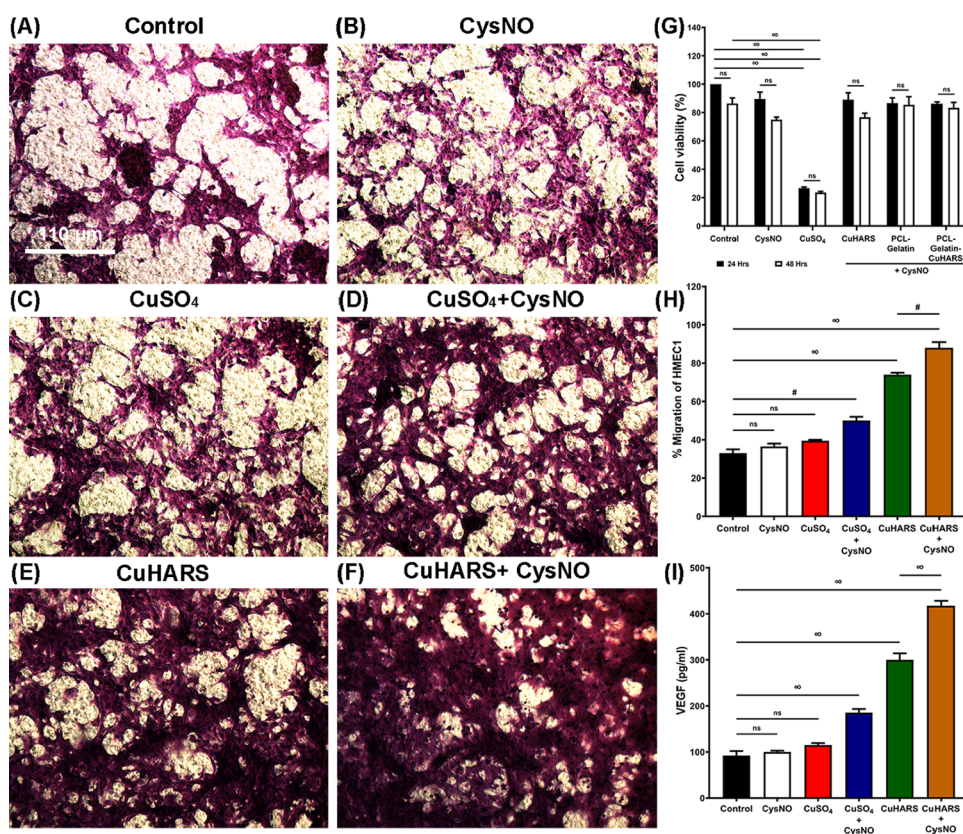


Figure 6. Migration ability and cell viability of HMEC1 in the presence of CysNO and CuHARS ($n = 3$). HMEC1 cells were plated on a 24-well transwell insert and cultured under different conditions to test their ability to migrate toward gradient for 24 h. Optical microscopy images showing migration of HMEC1 in (A) control, (B) 10 $\mu\text{M}/\text{mL}$ CysNO, (C) 10 $\mu\text{g}/\text{mL}$ CuSO₄, (D) 10 $\mu\text{g}/\text{mL}$ CuSO₄ + 10 $\mu\text{M}/\text{mL}$ CysNO, (E) 10 $\mu\text{g}/\text{mL}$ CuHARS, and (F) 10 $\mu\text{g}/\text{mL}$ CuHARS + 10 $\mu\text{M}/\text{mL}$ CysNO. (H) Graph showing the quantity of % migration under different conditions. (G) Graphical representation of cell viability of HMEC1. (I) Bar graph showing VEGF levels in conditioned media of HMEC1 under different treatments. p values calculated and denoted as ns ($p > 0.05$), * ($p \leq 0.05$), # ($p \leq 0.01$), and ∞ ($p \leq 0.001$).

underscores the continuous supply of elevated NO throughout the initial wound-healing phase.

3.5. Antibacterial Effect. NO and Cu²⁺ have already been recognized as effective antibacterial agents when employed individually.^{32,33,45,47,74,75} This study has demonstrated the existence of a synergistic antibacterial effect when elevated NO and Cu²⁺ levels are present concurrently, a phenomenon confirmed through *in vitro* testing. The progressive release of Cu²⁺ and its influence on NO catalysis played a pivotal role in the suppression of bacteria within the initial 4 h window when subjected to sonicated CuHARS or CuHARS embedded in PCL/gelatin aerogels. The results of the LIVE/DEAD assay present the percentage of decreased Methicillin-resistant *Staphylococcus aureus* (MRSA) for different experimental conditions. The control MRSA group exhibited only $2.52 \pm 0.44\%$ dead MRSA cells after 4 h of incubation at 37 °C. In contrast, MRSA cells treated with 10 μM CysNO, 10 $\mu\text{g}/\text{mL}$ sonicated CuHARS, 10 $\mu\text{g}/\text{mL}$ sonicated CuHARS + 10 $\mu\text{M}/\text{mL}$ CysNO, PCL/gelatin aerogels (without CuHARS) + 10 μM CysNO, and PCL/gelatin aerogels containing 10 μg CuHARS + 10 μM CysNO demonstrated 20.28 ± 0.41 , 14.67 ± 2.01 , 26.63 ± 0.98 , 18.44 ± 0.38 , and $22 \pm 0.59\%$ deceased MRSA cells, respectively, as depicted in Figure 5C. The NO generated solely from CysNO decomposition led to approximately 20% MRSA cell death. However, the catalytic synergy between NO and Cu²⁺, amplified by the presence of sonicated CuHARS, increased the bactericidal effect by an additional ~6%, elevating the cell death rate to ~26%. A similar

enhancement in bactericidal effect was observed in the case of PCL/gelatin aerogels containing CuHARS, again confirming the synergistic interplay between NO catalysis and Cu²⁺ to foster bactericidal efficiency. While the aerogel itself, with gelatin enveloping the CuHARS surface during initial hours, possibly mitigated the bactericidal effect, it still exhibited ~2% greater effectiveness than the treatment group containing CysNO alone. This unequivocally demonstrates the collaborative impact of NO catalysis with Cu²⁺, reinforcing the overall antibacterial efficacy.

The antibacterial effect, coupled with an inhibitory impact on MRSA's ability to proliferate, became evident when bacterial colonies from the experiment were replated on agar plates. In particular, notable suppression of MRSA colony formation was observed in the treatment groups involving CysNO and CuHARS, either in their raw material forms or incorporated within PCL/gelatin aerogels. The outcomes revealed that MRSA colonies replated from the following treatment groups: 10 μM CysNO, 10 $\mu\text{g}/\text{mL}$ sonicated CuHARS, 10 $\mu\text{g}/\text{mL}$ sonicated CuHARS + 10 μM CysNO, and PCL/gelatin aerogels containing 10 μg CuHARS + 10 μM CysNO, exhibited the higher degree of colony suppression. These groups demonstrated reductions of 69.69, 72.72, 61.90 and 53.67%, respectively, when compared to the number of MRSA colonies formed by the untreated control group, which was set at 100%, as illustrated in Figure S4. Notably, treatment groups that combined both CysNO and CuHARS showcased the greatest capacity for suppressing MRSA colonies, high-

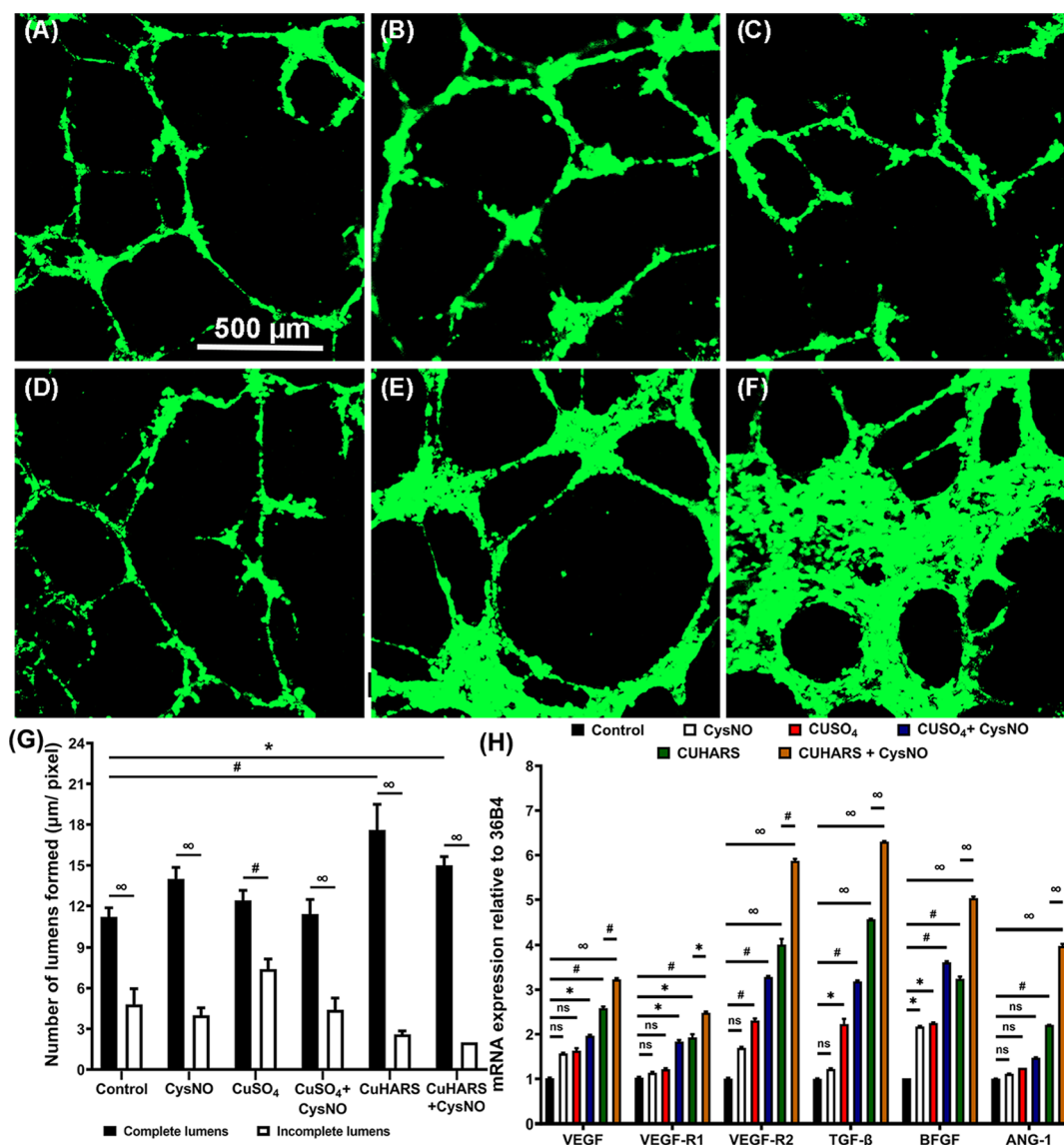


Figure 7. Effect of CysNO, CuHARS, and their synergistic effect on the formation of the lumen of HMEC1 cells plated on matrigel coated coverslips ($n = 3$). (A–D) Confocal images showing the lumen formation of HMEC1 (A) without treatment (Control), (B) treated with 10 μM /mL CysNO, (C) 10 $\mu\text{g}/\text{mL}$ sonicated CuSO_4 , (D) 10 $\mu\text{g}/\text{mL}$ sonicated CuSO_4 with 10 μM /mL CysNO (E) 10 $\mu\text{g}/\text{mL}$ sonicated CuHARS, and (F) 10 μM /mL CysNO along with 10 $\mu\text{g}/\text{mL}$ sonicated CuHARS. (G) The number of incomplete and complete lumens formed under different treatments. (H) Graphical representation of angiogenic gene expression in HMEC1 after treatment with 10 μM /mL CysNO, 10 $\mu\text{g}/\text{mL}$ CuSO_4 , 10 $\mu\text{g}/\text{mL}$ CuSO_4 + 10 μM /mL CysNO, 10 $\mu\text{g}/\text{mL}$ CuHARS, and 10 $\mu\text{g}/\text{mL}$ CuHARS + 10 μM /mL CysNO for 48 h and compared to the control. All values represented in the graph are normalized and shown relative to housekeeping gene 36B4. p values calculated and denoted as ns ($p > 0.05$), * ($p \leq 0.05$), # ($p \leq 0.01$), and ∞ ($p \leq 0.001$).

lighting the potential of CuHARS as a potent antibacterial agent. Our work solely considered the bacterial suppression at the initial scaffold implantation phase under endogenous levels of NO catalyzed from RSNOs present in blood simulated by CuHARS *in vitro*. We expect to see an enhanced antibacterial effect with a continuous supply of RSNOs from blood in the human body as it involves a continuous blood flow.

3.6. Cell Viability of HMEC1 in CuHARS. The CCK8 assay was used to evaluate the viability of HMEC1 cells *in vitro* under various experimental conditions. This assay revealed the proliferation and viability of cells in the presence of CuHARS. The viability of HMEC1 cells was examined for up to 48 h after introducing CuHARS into the culture wells. Within the test groups, which involved a combination of 10 μM /mL CysNO with 10 $\mu\text{g}/\text{mL}$ CuHARS, as well as PCL/gelatin

aerogels containing 10 μg CuHARS, viability percentages were quantified. At the 24 h mark, these groups demonstrated viabilities of 89.07 ± 8.46 and $86.26 \pm 2.1\%$, respectively, relative to the control normalized at 100%. This trend continued at the 48-h interval, with viabilities of 76.72 ± 4.91 and $83.36 \pm 6.75\%$, respectively, compared to control viability of $86.4 \pm 6.62\%$. The negative control, represented by CuSO_4 at a concentration of 10 $\mu\text{g}/\text{mL}$, exhibited significantly lower viabilities of 26.65 ± 1.46 and $23.64 \pm 1.39\%$ at the 24- and 48-h time points. This outcome suggests the toxic effects of copper-based salts under similar experimental conditions, as depicted in Figure 6G. Previous studies conducted by Darder et al. and Prajapati et al. on rat brain microvascular endothelial cells evaluated the cytotoxic impacts of CuHARS, indicating minimal to negligible toxicity toward these cells.^{45,46} Our

experimental setup produced similar results under parallel *in vitro* conditions. This outcome provides strong evidence of the biocompatibility of CuHARS as a biomaterial capable of donating Cu^{2+} . Consequently, CuHARS holds promise for potential *in vivo* applications in tissue regeneration, particularly in the realm of wound healing.

3.7. Migratory Ability of HMEC1 in CuHARS. Copper ions and NO are individually recognized as contributors to the activation of human microvascular endothelial cells, and the migration of activated endothelial cells is considered a positive marker for the formation of vascular structures in wound regions. In our study, we observed both the separate stimulations by CuHARS and NO on HMEC1, as well as the synergistic effect of elevated NO levels in the presence of Cu^{2+} on HMEC1 migration. Figure 6A–F shows HMEC1 migration under various experimental conditions. When compared to the control (Figure 6A,H), the CysNO and CuSO_4 groups showed no significant difference (Figure 6B,C,H). However, the CuSO_4 with CysNO group exhibited a slight increase in cell migration, approximately 45% (Figure 6D,H). Notably, CuHARS significantly enhanced HMEC1 migration, covering ~70% of the transwell insert bottom (Figure 6E,H). Among all groups, the CuHARS with CysNO group promoted the highest migratory response, with nearly 85% of cells migrated (Figure 6F,H), indicating a synergistic effect between CuHARS and NO. The presence of copper ions was identified as the most crucial factor in the *in vitro* migration assay. In a 24 h experiment, a burst of copper ions indicated faster HMEC1 migration, although the rapid formation and accumulation of copper(II) oxide were found to hinder lumen organization and cause apoptosis in endothelial cells.⁷⁶

The expression levels of VEGF, a well-known angiogenic factor were evaluated in the HMEC1-conditioned media under different experimental conditions. The results mirrored the trend observed in the migration study. We observed an increase in VEGF levels in the presence of CuSO_4 + CysNO compared to the control, CysNO, and CuSO_4 treatment conditions, attributed to the initial burst availability of Cu^{2+} due to dissociation of the copper salt (Figure 6I).

3.8. Formation of Lumens by HMEC1. The progression of wound healing and tissue regeneration involves the development of granular tissues and vascular tissues.^{24,69} The establishment of complete lumens by vascular endothelial cells in the wound region is pivotal for initial blood vessel outgrowth, which facilitates the transport of blood and nutrients to the regenerating tissue.^{77,78} To evaluate the formation of complete lumens in the presence of CuHARS and catalysis of NO, a tube formation assay was conducted—a widely used method for assessing *in vitro* angiogenesis. Figure 7 displays the number of incomplete versus complete lumens formed by human microvascular endothelial cells in the presence of CysNO, CuHARS, both CysNO and another source of copper, CuSO_4 . Confocal images of calcein-stained HMEC1 cells forming lumens during the tube assay are provided for various test conditions: untreated control, treated with 10 $\mu\text{M}/\text{mL}$ CysNO, 10 $\mu\text{g}/\text{mL}$ CuHARS, 10 $\mu\text{g}/\text{mL}$ CuSO_4 , 10 $\mu\text{g}/\text{mL}$ CuSO_4 with 10 $\mu\text{M}/\text{mL}$ CysNO, and 10 $\mu\text{M}/\text{mL}$ CysNO along with 10 $\mu\text{g}/\text{mL}$ CuHARS, illustrated in Figure 7A–F, respectively. The untreated control group exhibited a higher number of incomplete lumens and a lower number of complete lumens, resulting in a complete lumen formation percentage of 68.75%. Conversely, treatment groups

receiving 10 $\mu\text{M}/\text{mL}$ CysNO, 10 $\mu\text{g}/\text{mL}$ CuHARS, and 10 $\mu\text{M}/\text{mL}$ CysNO along with 10 $\mu\text{g}/\text{mL}$ CuHARS displayed an increased number of complete lumens and a reduction in incomplete lumens, leading to complete lumen formation percentages of 77.78, 85.71, and 88.24% respectively, as depicted in Figure 7G. The group treated with 10 $\mu\text{g}/\text{mL}$ CuSO_4 exhibited fewer complete lumens likely due to the potential cytotoxic effect of the salt. This effect slightly improved when 10 $\mu\text{M}/\text{mL}$ CysNO was introduced alongside 10 $\mu\text{g}/\text{mL}$ CuSO_4 . Initially, the NO generated from 10 $\mu\text{M}/\text{mL}$ CysNO assisted in forming a notable number of complete lumens. However, the highest ratio of complete to incomplete lumens emerged in the treatment group comprising 10 $\mu\text{g}/\text{mL}$ CuHARS and 10 $\mu\text{M}/\text{mL}$ CysNO. In this case, the presence of Cu^{2+} and elevated NO levels likely stimulated endothelial cells, aiding their migration and lumen formation. The synergistic action of NO from CysNO and CuHARS resulted in the fewest incomplete lumens within the treatment group of 10 $\mu\text{M}/\text{mL}$ CysNO along with 10 $\mu\text{g}/\text{mL}$ CuHARS, indicating a potential strategy for well-defined neovascularization during tissue regeneration. The treatment groups involving 10 $\mu\text{g}/\text{mL}$ CuSO_4 in the presence and absence of 10 $\mu\text{M}/\text{mL}$ CysNO did not perform well in tube assay due to the inherent toxicity of copper sulfate in comparison to CuHARS.

3.9. Angiogenic Gene Profile of HMEC1 in the Presence of CuHARS. To support our findings regarding lumen formation by HMEC1, we conducted an analysis of gene expression associated with angiogenesis. We evaluated the levels of VEGF, VEGF receptor 1 (VEGF-R1), VEGF-R2, transforming growth factor β (TGF- β), fibroblast growth factor basic (bFGF), and angiopoietin 1 (ANG 1) (Figure 7H). In comparison to the control group, VEGF levels remained consistent in the CysNO, CuSO_4 , and CuSO_4 with CysNO groups but exhibited higher levels in CuHARS-treated groups, both with and without CysNO. Interestingly, the RNA expression of VEGF-R1 and VEGF-R2 was elevated in the CuHARS-treated groups, with VEGF-R2 showing a particularly pronounced increase, nearly four-fold and six-fold in CuHARS and CuHARS with CysNO, respectively, compared to the control. Furthermore, VEGF-R2 expression was two-fold, three-fold, and four-fold higher than the control in the CysNO, CuSO_4 , and CuSO_4 with CysNO groups, respectively, while no significant change in VEGF-R1 expression was observed in these groups. These findings suggest that copper-induced cellular signaling in endothelial cells may operate through the VEGF and VEGF-R2 pathways, warranting further investigation to elucidate the underlying mechanisms.

Additionally, the impact of CuHARS on other potent angiogenic factors, namely TGF- β , bFGF, and ANG-1 was examined (Figure 7H). Compared to the control, most treatment groups, except for CysNO, exhibited an increase in TGF- β expression. RNA expression of bFGF was significantly elevated in all treatment groups. Conversely, ANG1 levels remained unchanged in CysNO, CuSO_4 , and CuSO_4 with CysNO relative to the control, but ANG1 expression increased twofold in CuHARS-treated groups, further escalating in CuHARS with CysNO. In conclusion, our study demonstrates that CuHARS promotes angiogenesis, as evidenced by lumen formation and the altered expression of genes associated with this process. CuHARS in conjunction with catalyzed NO generation, exhibits a synergistic effect, positioning CuHARS as a promising biomaterial in the field of tissue engineering.

4. CONCLUSIONS AND FUTURE WORK

We have successfully conducted a comprehensive characterization of CuHARS, delving into their physical and chemical attributes. Such an exploration is pivotal for any biomaterial intended for employment in the domains of wound healing and tissue regeneration. Our analysis encompassed the synthesis of CuHARS, shedding light on critical traits such as the existence of S–S bonds forming the backbone of the crystalline structure. These bonds serve to bridge the copper components, acting as a conduit for a MOB. This distinctive feature distinguishes CuHARS from porous MOFs. Notably, this marks the inaugural study involving the application of CuHARS as an active material. The incorporation of CuHARS into biomimetic PCL/gelatin nanofiber aerogels successfully established a contact source of copper, enabling the catalysis of elevated levels of NO from RSNOs. CuHARS demonstrated a potent burst bactericidal effect through the release of Cu²⁺, while simultaneously promoting the creation of lumens by microvascular endothelial cells, which is considered the initial phase of angiogenesis. Furthermore, the substantial levels of NO catalyzed from simulated RSNO in human blood showcased a synergistic impact. This synergy was observed in both the eradication of MRSA and the facilitation of endothelial cell migration, fostering successful lumen development. These outcomes suggest the potential utility of CuHARS in treating chronic wounds. This is particularly significant given that chronic wounds generally possess lower inflammatory stimuli, as indicated by NO generation, compared to acute wounds. The innovative concept presented in this research encompasses a twofold strategy, encompassing both bactericidal attributes and angiogenic potential through the utilization of this novel biomaterial. This breakthrough could hold promise for addressing chronic wounds and also offer an effective approach to acute wound treatment within a short time frame. CuHARS exhibits the qualities of being cost-effective, biocompatible, and biodegradable nanomaterials. They can be seamlessly integrated into various scaffold systems, including hydrogel-based platforms augmented with growth factors, thereby bolstering wound tissue regeneration endeavors. One of the major future tasks associated with this study involves testing aerogels *in vivo* using small animal wound models, especially in diabetic mice. The goal is to assess the efficacy of these scaffolds based on the results obtained from *in vitro* analyses. Another aspect of this work is to successfully represent the unit crystal structure of CuHARS through computational modeling. This representation opens up future opportunities to modify and add functional groups during the synthesis phase of the materials themselves for specific biomedical applications.

■ ASSOCIATED CONTENT

Data Availability Statement

The data that support the findings of this study are available from the corresponding author upon reasonable request.

SI Supporting Information

The Supporting Information is available free of charge at <https://pubs.acs.org/doi/10.1021/acsomega.3c10012>.

EDS analysis of CuHARS; EDS analysis of CuHARS embedded in PCL/gelatin aerogel; optical microscopy images illustrating the degradation of nonsonicated CuHARS; and MRSA colony formation after different treatments for 4 h (PDF)

■ AUTHOR INFORMATION

Corresponding Author

Jingwei Xie – Department of Surgery-Transplant and Holland Regenerative Medicine Program, University of Nebraska Medical Center, Omaha, Nebraska 68198, United States; Department of Mechanical and Materials Engineering, University of Nebraska Lincoln, Lincoln, Nebraska 68588, United States; orcid.org/0000-0002-8126-1397; Email: jingwei.xie@unmc.edu

Authors

Anik Karan – Department of Surgery-Transplant and Holland Regenerative Medicine Program, University of Nebraska Medical Center, Omaha, Nebraska 68198, United States;

orcid.org/0000-0002-5302-8408

Navatha Shree Sharma – Department of Surgery-Transplant and Holland Regenerative Medicine Program, University of Nebraska Medical Center, Omaha, Nebraska 68198, United States

Margarita Darder – Instituto de Ciencia de Materiales de Madrid (ICMM), CSIC, Madrid 28049, Spain;

orcid.org/0000-0002-7032-0419

Yajuan Su – Department of Surgery-Transplant and Holland Regenerative Medicine Program, University of Nebraska Medical Center, Omaha, Nebraska 68198, United States

Syed Muntazir Andrabi – Department of Surgery-Transplant and Holland Regenerative Medicine Program, University of Nebraska Medical Center, Omaha, Nebraska 68198, United States

S M Shatil Shahriar – Department of Surgery-Transplant and Holland Regenerative Medicine Program, University of Nebraska Medical Center, Omaha, Nebraska 68198, United States

Johnson V. John – Terasaki Institute for Biomedical Innovation, Los Angeles, California 90024, United States

Zeyu Luo – Division of Engineering in Medicine, Department of Medicine, Brigham and Women's Hospital, Harvard Medical School, Cambridge, Massachusetts 02139, United States

Mark A. DeCoster – Biomedical Engineering and Institute for Micromanufacturing, Louisiana Tech University, Ruston, Louisiana 71272, United States

Yu Shrike Zhang – Division of Engineering in Medicine, Department of Medicine, Brigham and Women's Hospital, Harvard Medical School, Cambridge, Massachusetts 02139, United States; orcid.org/0000-0002-0045-0808

Complete contact information is available at:

<https://pubs.acs.org/10.1021/acsomega.3c10012>

Author Contributions

○A.K. and N.S.S. contributed equally and are listed as co-first authors.

Notes

The authors declare no competing financial interest.

■ ACKNOWLEDGMENTS

This work was partially supported by startup funds from the University of Nebraska Medical Center (UNMC), National Institute of General Medical Science (NIGMS) of the National Institutes of Health under Award Numbers R01GM138552 (J.X.), Nebraska Research Initiative grant and NE LB606. Y.S.Z. acknowledges support from the Brigham Research

Institute. M.D. gratefully acknowledges support from MCIN/AEI/10.13039/501100011033 (Spain, project PID2019-105479RB-I00), the Fulbright Program and the Spanish Ministry of Education (grant PRX16/00153).

REFERENCES

- (1) Uauy, R.; Olivares, M.; Gonzalez, M. Essentiality of Copper in Humans. *Am. J. Clin. Nutr.* **1998**, *67* (5), 952S–959S.
- (2) Karlin, K.; Metalloenzymes, D. Structural Motifs, and Inorganic Models. *Science* (80-) **1993**, *261* (5122), 701–708.
- (3) Solomon, E. I.; Sundaram, U. M.; Machonkin, T. E. Multicopper Oxidases and Oxygenases. *Chem. Rev.* **1996**, *96* (7), 2563–2606.
- (4) Berends, H. P.; Stephan, D. W. Copper(I) and Copper(II) Complexes of Biologically Relevant Tridentate Ligands. *Inorg. Chim. Acta* **1984**, *93* (4), 173–178.
- (5) Murphy, B. P. Copper. *Coord. Chem. Rev.* **1993**, *124* (1–2), 63–105.
- (6) Yamauchi, O.; Odani, A.; Takani, M. Metal–Amino Acid Chemistry. Weak Interactions and Related Functions of Side Chain Groups. *J. Chem. Soc., Dalt. Trans.* **2002**, *18*, 3411–3421.
- (7) Kahler, H.; Lloyd, B. J.; Eden, M. Electron Microscopic and Other Studies on a Copper–Cystine Complex. *J. Phys. Chem.* **1952**, *56* (6), 768–770.
- (8) Hawkins, C. J.; Perrin, D. D. 255. Oxidation–Reduction Potentials of Metal Complexes in Water: Some Copper Complexes. *J. Chem. Soc.* **1962**, 1351–1357, DOI: 10.1039/JR9620001351.
- (9) Gale, R. J.; Winkler, C. A. Thermal Rearrangement of the Copper(II)-L-Cystine Complex. *Inorg. Chim. Acta* **1977**, *21*, 151–156.
- (10) Deodhar, S.; Huckaby, J.; Delahoussaye, M.; DeCoster, M. A. High-Aspect Ratio Bio-Metallic Nanocomposites for Cellular Interactions. *IOP Conf. Ser.: Mater. Sci. Eng.* **2014**, *64*, No. 012014.
- (11) Kelly, K.; Wasserman, J.; Deodhar, S. Generation of Scalable, Metallic High-Aspect Ratio Nanocomposites in a Biological Liquid Medium. *J. Vis. Exp.* **2015**, *8*, No. e52901.
- (12) Karan, A.; Darder, M.; Kansakar, U.; Norcross, Z.; DeCoster, M. Integration of a Copper-Containing Biohybrid (CuHARS) with Cellulose for Subsequent Degradation and Biomedical Control. *Int. J. Environ. Res. Public Health* **2018**, *15* (5), 844.
- (13) Zhang, M.; Gu, Z.-Y.; Bosch, M.; Perry, Z.; Zhou, H.-C. Biomimicry in Metal–Organic Materials. *Coord. Chem. Rev.* **2015**, *293–294*, 327–356.
- (14) Vaidhyanathan, R.; Bradshaw, D.; Rebilly, J.-N.; Barrio, J. P.; Gould, J. A.; Berry, N. G.; Rosseinsky, M. J. A Family of Nanoporous Materials Based on an Amino Acid Backbone. *Angew. Chem., Int. Ed.* **2006**, *45* (39), 6495–6499.
- (15) Manton, A.; Massüger, L.; Rabu, P.; Palivan, C.; McCusker, L. B.; Taubert, A. Metal–Peptide Frameworks (MPFs): “Bioinspired” Metal Organic Frameworks. *J. Am. Chem. Soc.* **2008**, *130* (8), 2517–2526.
- (16) Peri, D.; Ciston, J.; Gándara, F.; Zhao, Y.; Yaghi, O. M. Crystalline Fibers of Metal–Peptide Double Ladders. *Inorg. Chem.* **2013**, *52* (24), 13818–13820.
- (17) Martí-Gastaldo, C.; Warren, J. E.; Briggs, M. E.; Armstrong, J. A.; Thomas, K. M.; Rosseinsky, M. J. Sponge-Like Behaviour in Isorecticular Cu(Gly-His-X) Peptide-Based Porous Materials. *Chem. – Eur. J.* **2015**, *21* (45), 16027–16034.
- (18) Anderson, S. L.; Stylianou, K. C. Biologically Derived Metal Organic Frameworks. *Coord. Chem. Rev.* **2017**, *349*, 102–128.
- (19) Ferrari, R.; Bernés, S.; de Barbarin, C. R.; Mendoza-Diaz, G.; Gasque, L. Interaction between Glyglu and Ca²⁺, Pb²⁺, Cd²⁺ and Zn²⁺ in Solid State and Aqueous Solution. *Inorg. Chim. Acta* **2002**, *339*, 193–201.
- (20) Rabone, J.; Yue, Y.-F.; Chong, S. Y.; Stylianou, K. C.; Bacsa, J.; Bradshaw, D.; Darling, G. R.; Berry, N. G.; Khimyak, Y. Z.; Ganin, A. Y.; Wiper, P.; Claridge, J. B.; Rosseinsky, M. J. An Adaptable Peptide-Based Porous Material. *Science* **2010**, *329* (5995), 1053–1057.
- (21) Katsoulidis, A. P.; Park, K. S.; Antypov, D.; Martí-Gastaldo, C.; Miller, G. J.; Warren, J. E.; Robertson, C. M.; Blanc, F.; Darling, G. R.; Berry, N. G.; Purton, J. A.; Adams, D. J.; Rosseinsky, M. J. Guest-Adaptable and Water-Stable Peptide-Based Porous Materials by Imidazolate Side Chain Control. *Angew. Chem., Int. Ed.* **2014**, *53* (1), 193–198.
- (22) Carbonell, C.; Stylianou, K. C.; Hernando, J.; Evangelio, E.; Barnett, S. A.; Nettikadan, S.; Imaz, I.; Maspoch, D. Femtolitre Chemistry Assisted by Microfluidic Pen Lithography. *Nat. Commun.* **2013**, *4* (1), 2173.
- (23) Kaur, G.; Abramovich, L. A.; Gazit, E.; Verma, S. Ultrastructure of Metallopeptide-Based Soft Spherical Morphologies. *RSC Adv.* **2014**, *4* (110), 64457–64465.
- (24) Frykberg, R. G.; Banks, J. Challenges in the Treatment of Chronic Wounds. *Adv. Wound Care* **2015**, *4* (9), 560–582.
- (25) Zhao, Y.; Sultan, D.; Detering, L.; Cho, S.; Sun, G.; Pierce, R.; Wooley, K. L.; Liu, Y. Copper-64-Alloyed Gold Nanoparticles for Cancer Imaging: Improved Radiolabel Stability and Diagnostic Accuracy. *Angew. Chem., Int. Ed.* **2014**, *53* (1), 156–159.
- (26) Alliance of Wound Care Stakeholders Chronic Wounds: Economic Impact & Costs to Medicare. *Alliance Wound Care Stakeholders* **2018**, 15–18.
- (27) Nussbaum, S. R.; Carter, M. J.; Fife, C. E.; DaVanzo, J.; Haught, R.; Nusgart, M.; Cartwright, D. An Economic Evaluation of the Impact, Cost, and Medicare Policy Implications of Chronic Nonhealing Wounds. *Value Heal.* **2018**, *21* (1), 27–32.
- (28) Wo, Y.; Xu, L. C.; Li, Z.; Matzger, A. J.; Meyerhoff, M. E.; Siedlecki, C. A. Antimicrobial Nitric Oxide Releasing Surfaces Based on: S -Nitroso- N -Acetylpenicillamine Impregnated Polymers Combined with Submicron-Textured Surface Topography. *Biomater. Sci.* **2017**, *5* (7), 1265–1278.
- (29) Moreira, H. R.; Marques, A. P. Vascularization in Skin Wound Healing: Where Do We Stand and Where Do We Go? *Curr. Opin. Biotechnol.* **2022**, *73*, 253–262.
- (30) Tonnesen, M. G.; Feng, X.; Clark, R. A. F. Angiogenesis in Wound Healing. *J. Investig. Dermatology Symp. Proc.* **2000**, *5* (1), 40–46.
- (31) Rajpaul, K. Biofilm in Wound Care. *Br. J. Community Nurs.* **2015**, *20* (Sup3), S6–S11.
- (32) Xie, H.; Kang, Y. Role of Copper in Angiogenesis and Its Medicinal Implications. *Curr. Med. Chem.* **2009**, *16* (10), 1304–1314.
- (33) Jones, M. L.; Ganopolsky, J. G.; Labbé, A.; Wahl, C.; Prakash, S. Antimicrobial Properties of Nitric Oxide and Its Application in Antimicrobial Formulations and Medical Devices. *Appl. Microbiol. Biotechnol.* **2010**, *88* (2), 401–407.
- (34) Semisch, A.; Ohle, J.; Witt, B.; Hartwig, A. Cytotoxicity and Genotoxicity of Nano - and Microparticulate Copper Oxide: Role of Solubility and Intracellular Bioavailability. *Part. Fibre Toxicol.* **2014**, *11* (1), 10.
- (35) Hao, D.; Swindell, H. S.; Ramasubramanian, L.; Liu, R.; Lam, K. S.; Farmer, D. L.; Wang, A. Extracellular Matrix Mimicking Nanofibrous Scaffolds Modified With Mesenchymal Stem Cell-Derived Extracellular Vesicles for Improved Vascularization. *Front. Bieng. Biotechnol.* **2020**, *8*, 633.
- (36) Da, L. C.; Huang, Y. Z.; Xie, H. Q.; Zheng, B. H.; Huang, Y. C.; Du, S. R. Membranous Extracellular Matrix-Based Scaffolds for Skin Wound Healing. *Pharmaceutics* **2021**, *13* (11), 1796.
- (37) Alderton, W. K.; Cooper, C. E.; Knowles, R. G. Nitric Oxide Synthases: Structure, Function and Inhibition. *Biochem. J.* **2001**, *357* (3), 593.
- (38) Forstermann, U.; Sessa, W. C. Nitric Oxide Synthases: Regulation and Function. *Eur. Heart J.* **2012**, *33* (7), 829–837.
- (39) Andrabi, S. M.; Sharma, N. S.; Karan, A.; Shahriar, S. M. S.; Cordon, B.; Ma, B.; Xie, J. Nitric Oxide: Physiological Functions, Delivery, and Biomedical Applications. *Adv. Sci.* **2023**, *10*, No. 2303259.
- (40) Snyder, S. H.; Bredt, D. S. Biological Roles of Nitric Oxide. *Sci. Am.* **1992**, *266* (5), 68–77.

- (41) Bredt, D. S. Endogenous Nitric Oxide Synthesis: Biological Functions and Pathophysiology. *Free Radic. Res.* **1999**, *31* (6), 577–596.
- (42) Dulak, J.; Józkwicz, A.; Dembinska-Kiec, A.; Guevara, I.; Zdzenicka, A.; Zmudzinska-Grochot, D.; Florek, I.; Wójtowicz, A.; Szuba, A.; Cooke, J. P. Nitric Oxide Induces the Synthesis of Vascular Endothelial Growth Factor by Rat Vascular Smooth Muscle Cells. *Arterioscler. Thromb. Vasc. Biol.* **2000**, *20* (3), 659–666.
- (43) Cooke, J. P.; Losordo, D. W. Nitric Oxide and Angiogenesis. *Circulation* **2002**, *105* (18), 2133–2135.
- (44) Noiri, E.; Lee, E.; Testa, J.; Quigley, J.; Colflesh, D.; Keese, C. R.; Giaever, I.; Goligorsky, M. S. Podokinesis in Endothelial Cell Migration: Role of Nitric Oxide. *Am. J. Physiol. Physiol.* **1998**, *274* (1), C236–C244.
- (45) Darder, M.; Karan, A.; Real, G. D.; DeCoster, M. A. Cellulose-Based Biomaterials Integrated with Copper-Cystine Hybrid Structures as Catalysts for Nitric Oxide Generation. *Mater. Sci. Eng., C* **2020**, *108*, No. 110369.
- (46) Prajapati, N.; Karan, A.; Khezerlou, E.; DeCoster, M. A. The Immunomodulatory Potential of Copper and Silver Based Self-Assembled Metal Organic Biohybrids Nanomaterials in Cancer Theranostics. *Front. Chem.* **2021**, *8*, No. 629835.
- (47) Weng, L.; Boda, S. K.; Teusink, M. J.; Shuler, F. D.; Li, X.; Xie, J. Binary Doping of Strontium and Copper Enhancing Osteogenesis and Angiogenesis of Bioactive Glass Nanofibers While Suppressing Osteoclast Activity. *ACS Appl. Mater. Interfaces* **2017**, *9* (29), 24484–24496.
- (48) Vincent, M.; Duval, R. E.; Hartemann, P.; Engels-Deutsch, M. Contact Killing and Antimicrobial Properties of Copper. *J. Appl. Microbiol.* **2018**, *124* (5), 1032–1046.
- (49) Pham, A. N.; Xing, G.; Miller, C. J.; Waite, T. D. Fenton-like Copper Redox Chemistry Revisited: Hydrogen Peroxide and Superoxide Mediation of Copper-Catalyzed Oxidant Production. *J. Catal.* **2013**, *301*, 54–64.
- (50) Salah, I.; Parkin, I. P.; Allan, E. Copper as an Antimicrobial Agent: Recent Advances. *RSC Adv.* **2021**, *11* (30), 18179–18186.
- (51) Ray, P. D.; Huang, B.-W.; Tsuji, Y. Reactive Oxygen Species (ROS) Homeostasis and Redox Regulation in Cellular Signaling. *Cell. Signal.* **2012**, *24* (5), 981–990.
- (52) Stratton, C. W. Dead Bugs Don't Mutate: Susceptibility Issues in the Emergence of Bacterial Resistance. *Emerg. Infect. Dis.* **2003**, *9* (1), 10–16.
- (53) Hall, J. R.; Rouillard, K. R.; Suchyta, D. J.; Brown, M. D.; Ahonen, M. J. R.; Schoenfisch, M. H. Mode of Nitric Oxide Delivery Affects Antibacterial Action. *ACS Biomater. Sci. Eng.* **2020**, *6* (1), 433–441.
- (54) Fang, F. C. Mechanisms of Nitric Oxide-Related Antimicrobial Activity. *J. Clin. Invest.* **1997**, *99* (12), 2818–2825.
- (55) Privett, B. J.; Broadnax, A. D.; Bauman, S. J.; Riccio, D. A.; Schoenfisch, M. H. Examination of Bacterial Resistance to Exogenous Nitric Oxide. *Nitric Oxide - Biol. Chem.* **2012**, *26* (3), 169–173.
- (56) Karekar, N.; Karan, A.; Khezerlou, E.; Prajapati, N.; Pernici, C. D.; Murray, T. A.; DeCoster, M. A. Self-Assembled Metal–Organic Biohybrids (MOBs) Using Copper and Silver for Cell Studies. *Nanomaterials* **2019**, *9* (9), 1282.
- (57) Ravanbakhsh, H.; Luo, Z.; Zhang, X.; Maharjan, S.; Mirkarimi, H. S.; Tang, G.; Chávez-Madero, C.; Mongeau, L.; Zhang, Y. S. Freeform Cell-Laden Cryobioprinting for Shelf-Ready Tissue Fabrication and Storage. *Matter* **2022**, *5* (2), 573–593.
- (58) John, J. V.; McCarthy, A.; Wang, H.; Luo, Z.; Li, H.; Wang, Z.; Cheng, F.; Zhang, Y. S.; Xie, J. Freeze-Casting with 3D-Printed Templates Creates Anisotropic Microchannels and Patterned Macrochannels within Biomimetic Nanofiber Aerogels for Rapid Cellular Infiltration. *Adv. Healthc. Mater.* **2021**, *10* (12), No. 2100238.
- (59) Harding, J. L.; Reynolds, M. M. Metal Organic Frameworks as Nitric Oxide Catalysts. *J. Am. Chem. Soc.* **2012**, *134* (7), 3330–3333.
- (60) Socrates, G. *Infrared and Raman Characteristic Group Frequencies: Tables and Charts*, 3rd ed.; J Wiley and Sons: Chichester: West London, Middlesex, 2001.
- (61) Kominami, S.; Riesz, P.; Akiyama, T.; Silverton, J. V. X-Ray Diffraction and Electron Spin Resonance Studies of Single Crystals of Copper(II) Doped L-Cystine Dihydrochloride Dihydrate. *J. Phys. Chem.* **1976**, *80* (2), 203–210.
- (62) Ferrer, P.; da Silva, I.; Rubio-Zuazo, J.; Castro, G. R. Synthesis and Crystal Structure of the Novel Metal Organic Framework Zn(C₃H₅NO₂S)₂. *Powder Diffr.* **2014**, *29* (4), 366–370.
- (63) Pasquale, M. A.; Bolzán, A. E.; Güida, J. A.; Piatti, R. C. V.; Arvia, A. J.; Piro, O. E.; Castellano, E. E. A New Polymeric [Cu(SO₃(CH₂)₃S–S(CH₂)₃SO₃(H₂O)₄)_n Complex Molecule Produced from Constituents of a Super-Conformational Copper Plating Bath: Crystal Structure, Infrared and Raman Spectra and Thermal Behaviour. *Solid State Sci.* **2007**, *9* (9), 862–868.
- (64) Stanila, A.; Marcu, A.; Rusu, D.; Rusu, M.; David, L. Spectroscopic Studies of Some Copper(II) Complexes with Amino Acids. *J. Mol. Struct.* **2007**, *834–836*, 364–368.
- (65) Faust, B. *Modern Chemical Techniques*; The Royal Society of Chemistry, 1997.
- (66) Chaney, M. O.; Steinrauf, L. K. The Crystal and Molecular Structure of Tetragonal < scp > L-Cystine. *Acta Crystallogr. Sect. B Struct. Crystallogr. Cryst. Chem.* **1974**, *30* (3), 711–716.
- (67) Oughton, B. M.; Harrison, P. M. The Crystal Structure of Hexagonal L-Cystine. *Acta Crystallogr.* **1959**, *12* (5), 396–404.
- (68) Mohammed, A. V.; Arulappan, J. A. P.; Ganesand, S. T.; Sagadevane, S. Analysis on the Growth and Characterization of a Non-Linear Optical Single Crystal: L-Cystine Dihydrobromide. *Mater. Res.* **2015**, *18* (4), 828–832.
- (69) John, J. V.; Sharma, N. S.; Tang, G.; Luo, Z.; Su, Y.; Weihs, S.; Shahriar, S. M. S.; Wang, G.; McCarthy, A.; Dyke, J.; Zhang, Y. S.; Khademhosseini, A.; Xie, J. Nanofiber Aerogels with Precision Macrochannels and LL-37-Mimic Peptides Synergistically Promote Diabetic Wound Healing. *Adv. Funct. Mater.* **2023**, *33* (1), No. 2206936.
- (70) Hellman, N. E.; Gitlin, J. D. Ceruloplasmin Metabolism and Function. *Annu. Rev. Nutr.* **2002**, *22* (1), 439–458.
- (71) Løvstad, R. A. A Kinetic Study on the Distribution of Cu(II)-Ions between Albumin and Transferrin. *Biomaterials* **2004**, *17* (2), 111–113.
- (72) Shike, M. Copper in Parenteral Nutrition. *Gastroenterology* **2009**, *137* (5 SUPPL), S13–S17.
- (73) Ellingsen, D. G.; Horn, N.; Aaseth, J. Copper. In *Handbook on the Toxicology of Metals*; Elsevier, 2007; 529–546.
- (74) Schairer, D. O.; Chouake, J. S.; Nosanchuk, J. D.; Friedman, A. J. The Potential of Nitric Oxide Releasing Therapies as Antimicrobial Agents. *Virulence* **2012**, *3* (3), 271–279.
- (75) Pant, J.; Goudie, M. J.; Hopkins, S. P.; Brisbois, E. J.; Handa, H. Tunable Nitric Oxide Release from S-Nitroso-N-Acetylpenicillamine via Catalytic Copper Nanoparticles for Biomedical Applications. *ACS Appl. Mater. Interfaces* **2017**, *9* (18), 15254–15264.
- (76) Seo, Y.; Cho, Y. S.; Huh, Y. D.; Park, H. Copper Ion from Cu₂O Crystal Induces AMPK-Mediated Autophagy via Superoxide in Endothelial Cells. *Mol. Cells* **2016**, *39* (3), 195–203.
- (77) Eilken, H. M.; Adams, R. H. Dynamics of Endothelial Cell Behavior in Sprouting Angiogenesis. *Curr. Opin. Cell Biol.* **2010**, *22* (5), 617–625.
- (78) Rodrigues, M.; Kosaric, N.; Bonham, C. A.; Gurtner, G. C. Wound Healing: A Cellular Perspective. *Physiol. Rev.* **2019**, *99* (1), 665–706.